Available online at www.sciencedirect.com
ScienceDirect

Mathematics and Computers in Simulation 165 (2019) 280–305

MATHEMATICS AND COMPUTERS IN SIMULATION

www.elsevier.com/locate/matcom

Original articles

Channel flow simulation of a mixture with a full-dimensional generalized quasi two-phase model

Khim B. Khattri[a],*, Shiva P. Pudasaini[b]

[a] *Department of Mathematics, School of Science, Kathmandu University, Dhulikhel, Kavre, Nepal*
[b] *Institute of Geosciences and Meteorology, Geophysics Section, University of Bonn, Bonn, Germany*

Received 9 April 2018; received in revised form 4 January 2019; accepted 28 March 2019
Available online 10 April 2019

Abstract

We consider a newly constructed, mechanics-based, non-linear generalized quasi two-phase model [55] for a rapid flow of mixture of viscous fluid and solid particles down a channel. Based on the underlying physics and simulation results, we present new non-linear phenomena and mechanical insights of the model. We also present a full discretization of the model for the generalized mixture viscosity, velocity, pressure and effective bulk friction with higher order central differences and donor-cell method. This suitably tackles the complexities. Fundamentally new results are presented for the generalized mixture viscosity, velocity, pressure and effective bulk friction. Detailed analyses are performed for the full dimensional evolution of mixture velocities, dynamic pressure and effective viscosity. Our analysis reveals several mechanically very important novel non-linear features associated with the model under consideration, but often ignored in mass flow simulations, including: (i) The non-linear dynamics; as characterized by the flow mobility, kinetic energy, and the flow evolution are strongly controlled by the initial material composition. (ii) The flow becomes thicker as solid fraction increases, the front head develops into bulking, and the main body shows depletion. (iii) A strong velocity shearing develops through the flow depth. (iv) The full dynamic pressure exhibits strongly non-linear structures. (v) It appears that the hydrostatic pressure may significantly underestimate the full dynamic pressure. (vi) Mixture viscosity increases in different rates (slowly and rapidly) in different regimes of solid volume fractions which is justified by mechanical perspective of the mixture flow. (vii) The proper understanding of the incipient flow behavior is important, and shows that the process of flow release must be described by the full dimensional models. These features highlight the application potential of our new mixture mass flow model and simulation strategy for the hazard mitigation and planning.

Keywords: Mixture flow; Generalized bulk and shear viscosities; Generalized mixture velocities and pressure; Donor-cell discretization

1. Introduction

Debris flows are generally described as water saturated gravitational flows of solid particles [9,51,54]. Debris flows generally cause tremendous damages to people and infrastructures, agriculture fields and forests in most mountainous and hilly regions [26,69,70]. A typical debris flow that occurs in nature generally consists of unsteady

---

* Corresponding author.
E-mail address: khimkhattri@ku.edu.np (K.B. Khattri).

https://doi.org/10.1016/j.matcom.2019.03.014

and non-uniform surges of heterogeneous mixtures. The flow regimes may change significantly from initiation to run-out. Some local regions can be liquefied due to high fluid pressure or larger amount of fluid during the motion, while other regions may contain larger amount of solid or coarser material with high internal friction showing granular flow features [4,11,15,30,31,34] resulting in separation between solid and fluid-phases [62].

An empirical or dynamical (analytical) model can be used to predict mass flow dynamics. Empirical models are generally based on some limiting criteria or statistical relations, which may not capture the complex processes of debris flows completely. Continuum-mechanics based analytical models are mostly developed on the basis of the underlying physics and data, and are solved with suitable numerics. Appropriate rheological parameters of the considered mixtures, or fluids, are estimated by either a measurement-based approach or a calibration-based approach [49,53]. In a measurement-based approach, input parameters are obtained from controlled laboratory or field experiments on the involved material, which may not adequately reproduce the complex debris-flow properties, and scaling is another issue [11,49]. In a calibration-based approach, the rheological parameters are computed through the back analysis of full-scale or natural events [44,45]. Although this approach is simpler, the past debris flow events themselves may not be similar, or the potential events might differ substantially from the previous events on the same mountain slopes [46]. To address such difficulties, Pellegrino et al. [50] suggested an integrated approach that utilizes the laboratory experiment (e.g., for viscosity) and field investigation (e.g., for yield stress). Among the common rheologies for shear resistance, frictional, Voellmy, and quadratic rheology are applied that may depend on the normal load or flow depth and/or the shear-rate [47,53].

Model equations can be formulated in conservative or non-conservative forms. While they produce similar results for the smooth variation of the flow variables, conservative formulations produce much better simulations when rapid changes on the flow variables take place and the shock waves are generated, e.g., when the flow impacts the obstacles, or transits into deposition [37,45,56,58,68]. For shallow water flows, Schippa and Pavan [66] proposed a numerical model with a formulation for a set of conservative balance equations. This includes a particular mathematical expression for source terms to simulate hyperconcentrated flows in channels of complex geometry that results in increased numerical stability. Approaches adopting the balance equations with non-conservative source terms are also proposed [8,21,67]. However, the flow-fields computed from the conservative form of balance equations produce better results than from the non-conservative form. Numerical schemes developed for and applied to the conservative form of equations capture shocks often observed in geophysical mass flows [1,37,58], which, in general, is not the case with non-conservative formulations.

Other significant researches have also been carried out in the last few decades on debris flows and various models are developed from single-phase to two-phase. However, existing debris flow models still have significant limitations and many assumptions are required to cope with these extremely complex particle–fluid interactions in debris flows [7,36,38,53,57]. Examples include depth-averaged (reduced 2D) models [22,65], bulk mixture models, where particle and fluid move together [30,32], either simple dry Coulomb and Newtonian viscous fluid [54], or a single bulk rheology [35]. In some of the studies, debris flows have been treated as mixture flow of a single homogeneous material and non-Newtonian rheology has been employed to incorporate the effect of the particle interactions [30,33,65,69]. The depth-averaged mass and momentum conservation equations were introduced by Savage and Hutter [65], which were later utilized, modified, and extended by Denlinger and Iverson [12], and McDougall and Hungr [43]. The model of Savage and Hutter [65] was further extended to include the effects of pore fluid by Iverson and Denlinger [32], Pitman and Le [54], Pastor et al. [48], and Hutter and Schneider [24,25]. In these works, either effectively one-phase models are adopted, or they do not fully consider the two-phase nature of most mass flows and cannot describe fully the complex interactions between the particle and fluid and the explicit evolution and dynamics of the separate phases [44,45]. Simple drag was also incorporated in some models [27,29,54]. But, the generalized drag, which combines the solid-like and fluid-like drag contributions in the flow, and for both laminar and turbulent flows, has been developed by Pudasaini [57]. This model better describes the complex drag in mixture mass flows. Due to the non-zero relative acceleration, the virtual mass force is induced in the flow [57]. Similarly, the concentration gradient of the solid-phase induces the non-Newtonian viscous stress in the flow. Such essential physics of the two-phase flow were not included in the existing mass flow models.

Unifying three pioneering works, namely dry granular avalanche model of Savage and Hutter [65], debris mixture flow model of Iverson and Denlinger [32] and the two-fluid debris flow model of Pitman and Le [54], Pudasaini [57] developed a generalized two-phase theory for debris flow that reveals strong coupling between solid and fluid components through interfacial momentum transfer. The model includes buoyancy and several other important and dominant physical aspects of flow: enhanced non-Newtonian viscous stress induced by changes in the volume fraction of solid, virtual mass, and generalized drag [57]. This model constitutes the most generalized two-phase debris flow model to date and has further been enhanced and extended by Kattel et al. [38] to include the ambient drag and simulate glacial lake outburst flood (GLOF); by Pudassaini and Fischer [61,62] for erosion and phase-separation in two-phase flows, by Mergili et al. [44,45] for large scale field applications with cascades of debris flow events including erosion and mixing, and by Kattel et al. [37] and Kattel and Tuladhar [39] for fundamentally different obstacle-interactions of solid and fluid phases of debris mixture.

Existing models have further limitations. Depth-averaged approximations are mostly applicable to flows over smooth basal surfaces with no abrupt changes in slope. These approximations assume that the slope normal component of the velocity is negligible. However, when there are sharp gradients in the field variables (e.g., velocity, pressure and depth) the velocity shearing develops through the depth and thus is not uniform. Such phenomena are typically observed during the flow inception, flow-obstacle-interactions, and during deposition, and also in the case of converging and diverging flows [58]. For such situations, we need a physically complete description of the flow dynamics without depth averaging. Such dynamical models have been developed and applied by Domnik and Pudasaini [13] and Domnik et al. [14]; and further by von Boetticher et al. [72,73] for three dimensional flow. One of the major limitations of other existing models is the use of no-slip condition on the basal surface. Domnik et al. [14] proposed a fully two-dimensional, pressure and rate-dependent Coulomb-viscoplastic sliding model for granular-mixture flows. Following Pudasaini et al. [59], they show that no-slip boundary condition is, in general, not applicable to rapid granular and debris flows. They numerically studied granular flow down an inclined channel subject to Coulomb-slip at the bottom boundary with the marker-and-cell method. They showed that for Coulomb-viscoplastic sliding law, observable shearing mainly takes place close to the sliding surface, in agreement with observations. Similarly, von Boetticher et al. [73] developed a debris-mixture flow model. They utilized the pressure- and shear rate-dependent rheology so that the release dynamics and realistic deposit geometries can be achieved [72].

In order to perform a hazard assessment on a debris flow and design of the defense measures, estimation of the important parameters such as debris volume, flow velocity, peak discharge, runout distance and impact force on protection structures are needed which, however, is still challenging work [71]. In several studies, simple empirical relationships have been proposed to estimate these variables and rheological parameters [9,23,33,63]. In contrast, here, we consider a novel mechanics-based non-linear model [55] and present new full two-dimensional simulation on velocity and dynamic pressure fields for a debris mixture flow down a channel that substantially advances our understanding on complex mass flows with application potential. This motivated us to solve the non-linear mechanics based model numerically to highlight application potential with some benchmark simulations.

The new model [55] consists of two dimensional quasi two-phase mass and momentum equations for generalized mixture velocities and pressure. The model appears in non-conventional form due to the inertial coefficients, and the complex mixture viscosities. This structure resulted in the emergence of a new and dynamically evolving effective mixture friction coefficient, and general mixture viscosity, and reveals important mechanical aspects of the model. The model [55] has potentiality for wider applications, it will be computationally much faster than the full two-phase simulations, and at the same time, more accurate than the single-phase models. Another important aspect is that structurally, it is similar to the existing single phase granular or debris flow model [13,14] so that the same computational strategy can be applied to solve this new system. We use a staggered grid where mixture velocities and pressure are located at different grids. For diffusive terms, we use central difference whereas for convective terms, a combination of donor-cell and central difference is used. Here, we have discretized the Newtonian, Bingham, pressure dependent, and pressure-Poisson equations separately so that the same process can be used for the other reduced models. For visualization, we use a marker and cell (MAC) method, which is a finite difference scheme with an explicit first-order time discretization [19].

This work deals with the flow evolution from the silo gate down the channel. Detailed analyses are performed for the time evolution of full two dimensional (non depth-averaged) velocity and pressure fields for the full dynamical pressure, effective viscosity, and shear-rate. This allows us to analyze non-linear mechanics associated with the model and flow dynamics with respect to different initial solid volume fractions in the mixture from dilute to very dense flows. These flow dynamical quantities can play a decisive role for the constructions of defense structures for hazard mitigation in disaster prone mountains and coastal regions.

2. Model equations

The rapid motion of a debris flow in a channel is described by the bulk pressure p_m and the velocity $\mathbf{u}_m = (u_m, w_m)$, where u_m and w_m are the components in downslope (x) direction and perpendicular to the channel surface (z) (see, Fig. 5). The suffix m stands for mixture. The generalized quasi two-phase mixture model [55] consists of the following non-linear partial differential equations

$$\begin{aligned}\frac{\partial u_m}{\partial t} &+ \frac{\partial}{\partial x}(\Lambda_{uu} u_m^2) + \frac{\partial}{\partial z}(\Lambda_{uw} u_m w_m) = f_x - \frac{\partial p_m}{\partial x}\\ &+2\frac{\partial}{\partial x}\left[\Lambda_{\eta_u}\frac{\partial(\Lambda_u u_m)}{\partial x}\right] + \frac{\partial}{\partial z}\left[\Lambda_{\eta_u}\frac{\partial(\Lambda_u u_m)}{\partial z} + \Lambda_{\eta_w}\frac{\partial(\Lambda_w w_m)}{\partial x}\right],\end{aligned} \tag{1}$$

$$\begin{aligned}\frac{\partial w_m}{\partial t} &+ \frac{\partial}{\partial x}(\Lambda_{uw} u_m w_m) + \frac{\partial}{\partial z}(\Lambda_{ww}\, w_m^2) = f_z - \frac{\partial p_m}{\partial z}\\ &+\frac{\partial}{\partial x}\left[\Lambda_{\eta_u}\frac{\partial(\Lambda_u u_m)}{\partial z} + \Lambda_{\eta_w}\frac{\partial(\Lambda_w w_m)}{\partial x}\right] + 2\frac{\partial}{\partial z}\left[\Lambda_{\eta_w}\frac{\partial(\Lambda_w w_m)}{\partial z}\right],\end{aligned} \tag{2}$$

$$\frac{\partial^2 p_m}{\partial x^2} + \frac{\partial^2 p_m}{\partial z^2} = \frac{\partial F}{\partial x} + \frac{\partial G}{\partial z}, \tag{3}$$

where

$$F = -\frac{\partial}{\partial x}(\Lambda_{uu} u_m^2) - \frac{\partial}{\partial z}(\Lambda_{uw} u_m w_m) + 2\frac{\partial}{\partial x}\left[\Lambda_{\eta_u}\frac{\partial(\Lambda_u u_m)}{\partial x}\right] + \frac{\partial}{\partial z}\left[\Lambda_{\eta_u}\frac{\partial(\Lambda_u u_m)}{\partial z} + \Lambda_{\eta_w}\frac{\partial(\Lambda_w w_m)}{\partial x}\right] + f_x, \tag{4}$$

$$G = -\frac{\partial}{\partial x}(\Lambda_{uw} u_m w_m) - \frac{\partial}{\partial z}(\Lambda_{ww} w_m^2) + \frac{\partial}{\partial x}\left[\Lambda_{\eta_u}\frac{\partial(\Lambda_u u_m)}{\partial z} + \Lambda_{\eta_w}\frac{\partial(\Lambda_w w_m)}{\partial x}\right] + 2\frac{\partial}{\partial z}\left[\Lambda_{\eta_w}\frac{\partial(\Lambda_w w_m)}{\partial z}\right] + f_z. \tag{5}$$

In these equations, $\mathbf{f} = (f_x, f_z)$, where f_x and f_z are components of acceleration due to gravity. The momentum balance equations for the bulk mixture are represented by (1) and (2), and (3) is the pressure-Poisson equation that emerges from the mass and momentum balances. The third and fourth terms of (4)–(5) are due to the viscous deformation. The inertial and dynamical coefficients that appear in (1) and (2) are:

$$\begin{aligned}&\Lambda_{uu} = \frac{\alpha_s + \lambda_u^2\alpha_f}{(\alpha_s + \lambda_u\alpha_f)^2},\ \Lambda_{ww} = \frac{\alpha_s + \lambda_w^2\alpha_f}{(\alpha_s + \lambda_w\alpha_f)^2},\ \Lambda_{uw} = \frac{\alpha_s + \lambda_u\lambda_w\alpha_f}{(\alpha_s + \lambda_u\alpha_f)(\alpha_s + \lambda_w\alpha_f)},\ \Lambda_u = \frac{1}{\alpha_s + \lambda_u\alpha_f},\\ &\Lambda_w = \frac{1}{\alpha_s + \lambda_w\alpha_f},\ \Lambda_{\eta_u} = \nu_s\alpha_s + \lambda_u\nu_f\alpha_f,\ \Lambda_{\eta_w} = \nu_s\alpha_s + \lambda_w\nu_f\alpha_f,\ \Lambda_p = \alpha_s + \lambda_p\alpha_f,\end{aligned} \tag{6}$$

where, subscripts s and f represent the solid and fluid phases, α_s, $\alpha_f(= 1-\alpha_s)$ are solid and fluid volume fractions, λ_u, λ_w and λ_p are drift factors for velocities in x- and z-directions, and pressure, respectively [74,75]. The kinematic viscosity for fluid is given by ν_f and $\nu_s^e = \nu_s + \frac{\tau_{y_s}}{\|\mathbf{D}_m\|}\left(1 - e^{-m_y\|\mathbf{D}_m\|}\right)$ is the effective kinematic viscosity for solid, whereas ν_s is the kinematic viscosity for solid, $\tau_{y_s} = \tau_c + \tau_p p_m/\Lambda_p$ is the yield stress, τ_c is cohesion, $\tau_p p_m$ is pressure-dependent yield stress, m_y is a factor introduced for numerical purpose and $\mathbf{D}_m$ is the strain tensor. For the numerical integration of the model, these coefficients should be known, or parameterized. The set of equations (1)–(3) is a system of three highly non-linear partial differential equations in conservative form with three unknowns, namely, the mixture velocities, u_m, w_m, and the pressure p_m.

The main advantages of the model equations (1)–(3) are discussed in Pokhrel et al. [55]. From a numerical and simulation point of view, the computational cost of this generalized quasi-two-phase bulk mixture model is reduced drastically as compared to the two-phase model. This can be perceived qualitatively as the number of output variables is reduced from six to three, and also the interfacial interactions between the solid and the fluid phases are substantially reduced. Once u_m, w_m and p_m are obtained from (1)–(3), the two-phase dynamics of solid $(u_s, w_s;\, p_s)$ and fluid $(u_f, w_f;\, p_f)$ can be calculated from the relations $u_f = \lambda_u u_s$, $w_f = \lambda_w w_s$; $p_f = \lambda_p p_s$, and the definition of the bulk velocities, and the pressure of mixture flows:

$$u_m = (\alpha_s + \lambda_u\alpha_f)u_s,\quad w_m = (\alpha_s + \lambda_w\alpha_f)w_s,\quad p_m = (\alpha_s + \lambda_p\alpha_f)p_s\,\cdot \tag{7}$$

As derived from the general two-phase model of Pudasaini [57], and as an extension of Pokhrel et al. [55], Khattri and Pudasaini [41] have very recently derived an extended quasi two-phase mass flow model that includes further essential physics of two-phase mass flow model, such as generalized drag, virtual mass force and non-Newtonian viscous stress. The full discretization of these models and their simulations will be presented in some other possible contributions.

In structure, the system (1)–(3) is very much similar to the model developed by Domnik and Pudasaini [13]. However, here,

$$\Lambda_{\eta_m} = \frac{1}{2}\nu_s^e \alpha_s\left(\Lambda_u + \Lambda_w\right) + \frac{1}{2}\nu_f \alpha_f\left(\lambda_u \Lambda_u + \lambda_w \Lambda_w\right) \tag{8}$$

is the bulk viscosity that captures the mechanics of mixture rheology, which is a major advancement of this model. α_s (the effect of) enters into the model equations via inertial and dynamical coefficients; pressure parameters, velocity and pressure definitions (6)–(7). As these coefficients enhance the mass and momentum fluxes, these coefficients are applicable for any α_s values that change the fluxes. Importantly, the rheology defines and controls the flow behavior and flow regime in mixture flow. As the newly constructed viscosity combines the effective solid and fluid viscosities of the components in mixture, depending on the solid volume fraction, the mixture behaves as a dry granular flow ($\alpha_s \to 1$) then $\Lambda_{\eta_m} = \nu_s^e = \nu_s + \frac{\tau_{y_s}}{\|\mathbf{D}_m\|}\left(1 - e^{-m_y\|\mathbf{D}_m\|}\right)$; and that the material deforms as the pressure and rate-dependent Coulomb viscoplastic material [13,14,72,73]. This defines the mechanically strong frictional-viscous flow regime. In contrast, at a vanishing solid volume fraction ($\alpha_s \to 0$), $\Lambda_{\eta_m} = \nu_f$, the classical viscous fluid regime. Moreover, for $0 < \alpha_s < 1$, the mixture viscosity (8) continuously covers the whole spectrum of rheological behavior, from very dilute (fluid dominated) to very dense (solid dominated) mixture flow regime. This is a great advantage of the new formulation of the mixture flow model. As we will see later, Fig. 14 explains behavior of regime changes.

In order to highlight the basic and essential mechanics and explore important dynamics and application potential of the generalized model (1)–(3), here we focus only on some reduced form of (1)–(3). For the sake of simplicity, we set the velocity and pressure drifts close to unity, i.e., $\lambda_u, \lambda_w, \lambda_p \approx 1$ [55]. Now, (1)–(3) take the following reduced form of the model:

$$\frac{\partial u_m}{\partial t} + \frac{\partial (u_m^2)}{\partial x} + \frac{\partial (u_m w_m)}{\partial z} = f_x - \frac{\partial p_m}{\partial x} + 2\frac{\partial}{\partial x}\left(\Lambda_m \frac{\partial u_m}{\partial x}\right) + \frac{\partial}{\partial z}\left[\Lambda_m\left(\frac{\partial u_m}{\partial z} + \frac{\partial w_m}{\partial x}\right)\right], \tag{9}$$

$$\frac{\partial w_m}{\partial t} + \frac{\partial (u_m w_m)}{\partial x} + \frac{\partial (w_m^2)}{\partial z} = f_z - \frac{\partial p_m}{\partial z} + \frac{\partial}{\partial x}\left[\Lambda_m\left(\frac{\partial u_m}{\partial z} + \frac{\partial w_m}{\partial x}\right)\right] + 2\frac{\partial}{\partial z}\left(\Lambda_m \frac{\partial w_m}{\partial z}\right), \tag{10}$$

$$\frac{\partial^2 p_m}{\partial x^2} + \frac{\partial^2 p_m}{\partial z^2} = \frac{\partial F}{\partial x} + \frac{\partial G}{\partial z}, \tag{11}$$

where $\Lambda_m = \nu_s^e \alpha_s + \nu_f \alpha_f$ is the reduced effective mixture viscosity. In the limit as $\alpha_s \to 1$ (*i.e.*, $\alpha_f \to 0$), the solid–fluid mixture debris bulk changes into an effectively single phase granular flow and thus the model equations reduce to those in Domnik and Pudasaini [13] and Domnik et al. [14]. However, the new model equations (1)–(3) are much more general than Domnik and Pudasaini [13] and Domnik et al. [14] as they include inertial and dynamical coefficients (6), including complex mixture viscosity, in terms of solid and fluid volume fractions, and velocity and pressure drifts: α_s, α_f, λ_u, λ_w, λ_p.

In (9)–(10), the bulk viscosity (8) has further been reduced to simple mixture viscosity, Λ_m. In von Boetticher et al. [72,73], the effective mixture viscosity has been expressed as a linear combination between phase viscosities. But in the formulation of Pokhrel et al. [55] model, the mixture viscosities are more complex and non-linear combination between the phase viscosities as evident from (8). This makes the bulk viscosity to perform effectively for any mixture composition, from dilute to dense, even in the reduced situation.

von Boetticher et al. [73] presented one of the very first full dimensional debris bulk mixture simulations. There are some similarities between the model (1)–(3), and the model in von Boetticher et al. [73]. However, there are also some fundamental differences between these two models. Further difference lies in the applied numerical method and schemes. To simulate complex three-dimensional flow structures, von Boetticher et al. [73] used the volume-of-fluid approach, that combines the mixed phase and the air phase into a single cell-averaged Navier–Stokes equations for incompressible flow. The computational code is based on the open source CFD software, OpenFOAM. But, our numerical method is based on extended *NaSt2D* [13,14,17], which is an expanded computer code using the finite-volume method for the simulation of complex mixture consisting of incompressible non-Newtonian fluids and granular particles. Furthermore, both Domnik and Pudasaini [13] and von Boetticher et al. [73] models implement the bottom boundary as pressure- and rate-dependent Coulomb-viscoplastic slip conditions

[14] that evolve automatically as the flow moves downslope. However, the "effective bulk friction coefficient" is newly constructed in Pokhrel et al. [55] that includes the frictional and viscous properties and dynamics of both the solid and fluid phases as clearly seen in the mixture viscosity Λ_m.

In order to make the model discretization and simulation convenient, we express the force terms in the momentum equations (1) and (2) into Newtonian-type, Bingham and pressure and rate dependent terms as discussed below. With Λ_{η_m} in (8), the Cauchy stress tensor $\boldsymbol{\sigma}_m$ can be written as

$$\begin{aligned}\boldsymbol{\sigma}_m &= -p_m\mathbf{I} + 2\Lambda_{\eta_m}\mathbf{D}_m\\ &= -p_m\mathbf{I} + \nu_s\alpha_s\mathbf{D}_m(\Lambda_u+\Lambda_w) + \nu_f\alpha_f\mathbf{D}_m(\lambda_u\Lambda_u+\lambda_w\Lambda_w) + \nu_D\alpha_s\tau_c(\Lambda_u+\Lambda_w)\mathbf{D}_m + \nu_{\mathbf{D}}\alpha_s\tau_p p_m(\Lambda_u+\Lambda_w)\mathbf{D}_m,\end{aligned}$$

where, $\mathbf{D}_m = \frac{1}{2}\left[\nabla\mathbf{u}_m^{\Lambda} + (\nabla\mathbf{u}_m^{\Lambda})^T\right]$ is the (deformation) strain-rate tensor, $\mathbf{u}_m^{\Lambda} = (\Lambda_u u_m, \Lambda_w w_m)$ and ν_D is a function of norm of strain rate tensor, $\nu_D = f_\nu(\|D_m\|)$ with $f_\nu(\|D_m\|) = (1-\exp(-m_y\|D_m\|))/\|D_m\|$. The stress tensor $\boldsymbol{\sigma}_m$ can be decomposed into a Newtonian-type $\boldsymbol{\sigma}_m^N = -p_m\mathbf{I} + (\nu_s\alpha_s + \nu_f\alpha_f\lambda_u)(\Lambda_u+\Lambda_w)\mathbf{D}_m$, a Bingham-type $\boldsymbol{\sigma}_m^B = \nu_D\alpha_s\tau_c(\Lambda_u+\Lambda_w)\mathbf{D}_m$, and a pressure dependent part $\boldsymbol{\sigma}_m^P = \nu_D\alpha_s\tau_p p_m(\Lambda_u+\Lambda_w)\mathbf{D}_m$, as

$$\boldsymbol{\sigma}_m = \boldsymbol{\sigma}_m^N + \boldsymbol{\sigma}_m^B + \boldsymbol{\sigma}_m^P\cdot \tag{12}$$

The divergence of (12) gives the associated surface force contribution

$$\operatorname{div}\boldsymbol{\sigma}_m = (F, G) = (\mathcal{F}^N + \mathcal{F}^B + \mathcal{F}^P, \mathcal{G}^N + \mathcal{G}^B + \mathcal{G}^P), \tag{13}$$

as the sum of the Newtonian $(\mathcal{F}^N, \mathcal{G}^N)$, Bingham $(\mathcal{F}^B, \mathcal{G}^B)$ and pressure and rate-dependent $(\mathcal{F}^P, \mathcal{G}^P)$ force components. The Newtonian force components can be written as

$$\mathcal{F}^N = -\frac{\partial}{\partial x}(\Lambda_{uu}u_m^2) - \frac{\partial}{\partial z}(\Lambda_{uw}u_m w_m) + f_x + 2\frac{\partial}{\partial x}\left[\Lambda_{\eta_u}\frac{\partial}{\partial x}(\Lambda_u u_m)\right] + \frac{\partial}{\partial z}\left[\Lambda_{\eta_u}\frac{\partial}{\partial z}(\Lambda_u u_m) + \Lambda_{\eta_w}\frac{\partial}{\partial x}(\Lambda_w w_m)\right], \tag{14}$$

$$\mathcal{G}^N = -\frac{\partial}{\partial x}(\Lambda_{uw}u_m w_m) - \frac{\partial}{\partial z}(\Lambda_{ww}w_m^2) + f_z + 2\frac{\partial}{\partial z}\left[\Lambda_{\eta_u}\frac{\partial}{\partial x}(\Lambda_w w_m)\right] + \frac{\partial}{\partial x}\left[\Lambda_{\eta_u}\frac{\partial}{\partial z}(\Lambda_u u_m) + \Lambda_{\eta_w}\frac{\partial}{\partial x}(\Lambda_w w_m)\right], \tag{15}$$

which, for simplicity, also include gravity components. The Bingham force components can be written as

$$\mathcal{F}^B = \frac{\partial}{\partial x}(\boldsymbol{\sigma}_m^B)_{xx} + \frac{\partial}{\partial z}(\boldsymbol{\sigma}_m^B)_{xz}, \tag{16}$$

$$\mathcal{G}^B = \frac{\partial}{\partial x}(\boldsymbol{\sigma}_m^B)_{xz} + \frac{\partial}{\partial z}(\boldsymbol{\sigma}_m^B)_{zz}. \tag{17}$$

The pressure dependent force components in (13) can be written as

$$\mathcal{F}^P = p_m f_0 + f_x\frac{\partial p_m}{\partial x} + f_z\frac{\partial p_m}{\partial z}, \tag{18}$$

$$\mathcal{G}^P = p_m g_0 + g_x\frac{\partial p_m}{\partial x} + g_z\frac{\partial p_m}{\partial z}, \tag{19}$$

where

$$\begin{aligned}f_0 &= \tau_p\left[\frac{\partial}{\partial x}(\nu_D\alpha_s(\Lambda_u+\Lambda_w)(D_m)_{xx}) + \frac{\partial}{\partial z}(\nu_D\alpha_s(\Lambda_u+\Lambda_w)(D_m)_{xz})\right],\\ f_x &= \tau_p\nu_D\alpha_s(\Lambda_u+\Lambda_w)(D_m)_{xx},\\ f_z &= \tau_p\nu_D\alpha_s(\Lambda_u+\Lambda_w)(D_m)_{xz},\\ g_0 &= \tau_p\left[\frac{\partial}{\partial x}(\nu_D\alpha_s(\Lambda_u+\Lambda_w)(D_m)_{xz}) + \frac{\partial}{\partial z}(\nu_D\alpha_s(\Lambda_u+\Lambda_w)(D_m)_{zz})\right],\\ g_x &= \tau_p\nu_D\alpha_s(\Lambda_u+\Lambda_w)(D_m)_{xz},\\ g_z &= \tau_p\nu_D\alpha_s(\Lambda_u+\Lambda_w)(D_m)_{zz}\cdot\end{aligned}$$

Boundary Conditions: The boundary conditions are required on the computational variables u_m, w_m and p_m to numerically integrate the model equations (1)–(3). The free surface of the mass flow is traction free. Further, even the lowest layer in contact with bottom boundary moves with a slip velocity which is non-zero and non-trivial.

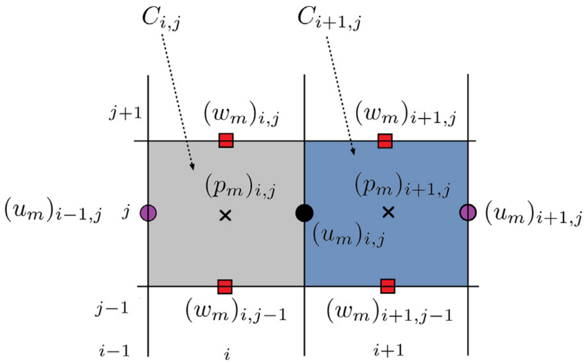

Fig. 1. The background colors gray and blue represent the cells $C_{i,j}$ and $C_{i+1,j}$ respectively. The cell $(i, j) = C_{i,j}$ occupies the spatial region $[(i-1)\delta x, i\delta x] \times [(j-1)\delta z, j\delta z]$ and the corresponding index (i, j) is assigned to the pressure, p_m at the cell center, u_m at the right edge and w_m at the upper edge of the cell $C_{i,j}$.

The non-zero slip velocity is determined by the frictional strength of the debris material, that depends on the load exerted by the material on the rigid boundary [13,14]. The condition for the bottom boundary as indicated by b can be achieved by the widely used Coulomb sliding law for bulk:

$$T_m^b = \frac{u_m^b}{|\mathbf{u}_m^b|} \tan\delta_m N_m^b, \tag{20}$$

where T_m^b is the shear stress, N_m^b is the normal load at the base, δ_m is the bed friction angle and $\mathbf{u}_m^b$ is the velocity of the bulk at the base. The basal boundary is assumed to be non penetrating. So, $\mathbf{n}\cdot\mathbf{u}_m^b = 0$ and also $[(\mathbf{t}\cdot\nabla)(\mathbf{n}\cdot\mathbf{u}_m)]^b = 0$, where $\mathbf{n}$ and $\mathbf{t}$ are normal and tangential vectors respectively on sliding plane. Now, the relation between the tangential and normal components of the flow at the base when used in (20) gives

$$\left(\frac{\partial u_m}{\partial z}\right)^b - 2c_m^F \left(\frac{\partial u_m}{\partial x}\right)^b = \frac{c_m^F}{\Lambda_{\eta_m}^b} p_m^b = F_{e_m}^r p_m^b, \tag{21}$$

where $F_{e_m}^r$ is the effective friction ratio, and the friction factor $c_m^F = \dfrac{u_m^b}{|\mathbf{u}_m^b|}\tan\delta_m$, if $u_m^b \neq 0$, otherwise 0. The pressure and rate-dependent Coulomb-viscoplastic sliding law for generalized bulk mixture (21) dynamically defines the bottom boundary velocity u_m^b [13]. This resulted in the extended pressure- and rate-dependent Coulomb-viscoplastic granular flow rheology (21) to debris mixture flow. Equation (21) is for describing the pressure in terms of velocity gradient or vice-versa [13]. We further employ the von Neumann boundary condition for the pressure by applying the momentum conservation in the direction of the normal at the rigid boundaries, i.e.,

$$\mathbf{n}\cdot\nabla p_m = \mathbf{n}\cdot\mathbf{F}, \tag{22}$$

where $\mathbf{F} = (F, G)$ is defined in (4) and (5).

3. Model discretization

The numerical treatment is based on the finite volume scheme [13,17]. Such schemes are beneficial for rapid flows and large deformations. The flow domain is discretized into $i_{\max}$ cells of equal sizes in the x-direction and similar $j_{\max}$ cells in the z-direction. The region is discretized using a staggered grid (Fig. 1), in which the pressures p_m are located at the cell centers, the horizontal velocities u_m at the midpoints of the vertical cell edges, and the vertical velocities w_m at the midpoints of the horizontal cell edges. Because of this choice, the discrete values of u_m, w_m and p_m are exactly located on three separate grids, each shifted by half a grid spacing to the bottom, to the left, and to the lower left respectively. Due to this shifting, all external grid points are not located on the domain boundary. So, extra boundary strips of grid cells are introduced all around the domain so that the boundary condition may be applied now by averaging the nearest grid points on either side. This staggered arrangement of the unknowns prevents possible pressure oscillations, which could have occurred if we had evaluated all unknown values u_m, w_m,

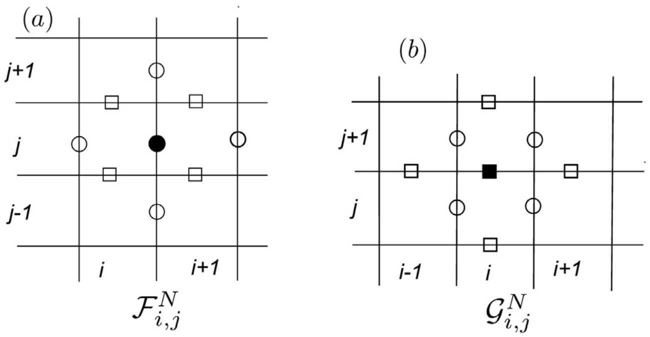

Fig. 2. Discretization of Newtonian terms: The filled circle and rectangle represent the discretization points of $\mathcal{F}^N_{i,j}$ and $\mathcal{G}^N_{i,j}$ respectively. Open circles represent u_m-velocities and squares represent w_m-velocities.

and p_m at the same grid points [13,17]. The discretization of α_s, Λ_u, Λ_w and $\|\mathbf{D}_m\|$ is also incorporated in this work, which is different from those in previous models. Here, we present the full discretization of the model (1)–(3) so that the associated numerics can also be applied to any form of full, or reduced models in Pokhrel et al. [55].

3.1. Discretization of force terms

Here, we present the discretization of the Newtonian, Bingham, and pressure-dependent terms.

3.1.1. Discretization of Newtonian terms

Because the convective terms in the momentum equations (first and second terms of the right hand side of (14) and (15)) become dominant at high velocities, it is beneficial to use a mixture of the central difference and the donor-cell discretization. The first term on the right hand side of (14) for u_m is discretized at the midpoint of the vertical cell edges (Fig. 2a) and the second term on the right hand side of (14) is discretized at the midpoint of the horizontal cell edges (Fig. 2b). So, the first and second terms in (14) are discretized at the midpoint of the right edge cell (i, j), by the combination of the central scheme and donor cell (associated with γ), and results in

$$\begin{aligned}
\left[\frac{\partial}{\partial x}(\Lambda_{uu}u_m^2)\right]_{i,j} = \frac{1}{\delta x}\Bigg[&(\Lambda_{uu})_{i+1,j}\left(\frac{(u_m)_{i,j}+(u_m)_{i+1,j}}{2}\right)^2-(\Lambda_{uu})_{i,j}\left(\frac{(u_m)_{i-1,j}+(u_m)_{i,j}}{2}\right)^2\\
&+\gamma\,|(\Lambda_{uu})_{i+1,j}|\left|\frac{(u_m)_{i,j}+(u_m)_{i+1,j}}{2}\right|\left(\frac{(u_m)_{i,j}-(u_m)_{i+1,j}}{2}\right)\\
&-\gamma\,|(\Lambda_{uu})_{i,j}|\left|\frac{(u_m)_{i-1,j}+(u_m)_{i,j}}{2}\right|\left(\frac{(u_m)_{i-1,j}-(u_m)_{i,j}}{2}\right)\Bigg],
\end{aligned}\tag{23}$$

$$\begin{aligned}
\left[\frac{\partial}{\partial z}(\Lambda_{uw}u_m w_m)\right]_{i,j} = \frac{1}{\delta z}\Bigg[&(\Lambda_{uw})_{i,j+1}\left(\frac{(w_m)_{i,j}+(w_m)_{i+1,j}}{2}\right)\left(\frac{(u_m)_{i,j}+(u_m)_{i,j+1}}{2}\right)\\
&-(\Lambda_{uw})_{i,j}\left(\frac{(w_m)_{i,j-1}+(w_m)_{i+1,j-1}}{2}\right)\left(\frac{(u_m)_{i,j-1}+(u_m)_{i,j}}{2}\right)\\
&+\gamma\,|(\Lambda_{uw})_{i,j+1}|\left|\frac{(w_m)_{i,j}+(w_m)_{i+1,j}}{2}\right|\left(\frac{(u_m)_{i,j}-(u_m)_{i,j+1}}{2}\right)\\
&-\gamma\,|(\Lambda_{uw})_{i,j}|\left|\frac{(w_m)_{i,j-1}+(w_m)_{i+1,j-1}}{2}\right|\left(\frac{(u_m)_{i,j-1}-(u_m)_{i,j}}{2}\right)\Bigg].
\end{aligned}\tag{24}$$

Other convective terms are discretized in the similar manner. Since central difference provides a higher order discretization, this may cause instabilities [13,17]. This instability can be avoided by using a mixture of central difference and donor-cell discretization through the donor cell parameter $\gamma \in [0, 1]$, as the donor cell scheme provides a stable discretization of lower order. If $\gamma = 1$, a pure donor cell is obtained and when $\gamma = 0$, the convective derivatives are discretized by pure central difference. The value of γ should be chosen according to the

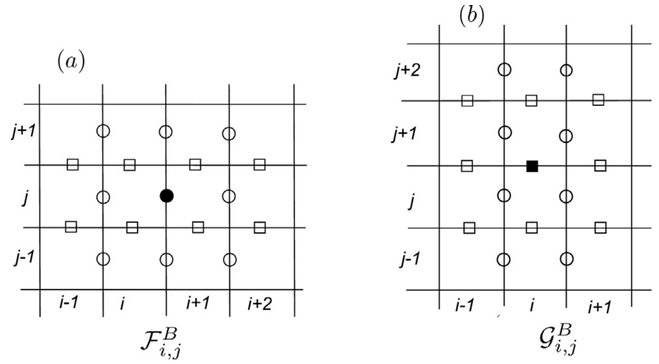

Fig. 3. Discretization of Bingham terms: The filled circle and rectangle represent the discretization points of $\mathcal{F}^B_{i,j}$ and $\mathcal{G}^B_{i,j}$ respectively. Open circles represent u_m-velocities and squares represent w_m-velocities.

dimensions of the convective terms relative to the diffusive ones [17]. According to Hirt et al. [20], γ should be chosen such that

$$\gamma \geq \max_{i,\,j}\left(\left|\frac{(u_m)_{\,i,j}\,\delta t}{\delta x}\right|,\left|\frac{(w_m)_{\,i,j}\,\delta t}{\delta z}\right|\right) \tag{25}$$

is satisfied, where δx and δz are mesh-width in x- and z-directions, δt is time step size.

The last two terms on the right hand side of (14) and (15) are discretized using central difference, e.g.,

$$\frac{\partial}{\partial x}\left[\Lambda_{\eta_u}\frac{\partial}{\partial x}(\Lambda_u u_m)\right]_{i,j} = \frac{1}{\delta x^2}\left[(\Lambda_{\eta_u})_{i+1,j}\left((\Lambda_u u_m)_{i+1,j}-(\Lambda_u u_m)_{i,j}\right)-(\Lambda_{\eta_u})_{i,j}\Big((\Lambda_u u_m)_{i,j}-(\Lambda_u u_m)_{i-1,j}\Big)\right]\cdot \tag{26}$$

3.1.2. Discretization of Bingham terms

Central difference is used for the discretization of the Bingham force terms, $\mathcal{F}^B$ in (16):

$$\mathcal{F}^B_{i,j} = \frac{1}{\delta x}\Big([(\boldsymbol{\sigma}^B_m)_{xx}]^p_{i+1,j} - [(\boldsymbol{\sigma}^B_m)_{xx}]^p_{i,j}\Big) + \frac{1}{\delta z}\Big([(\boldsymbol{\sigma}^B_m)_{xz}]^c_{i,j} - [(\boldsymbol{\sigma}^B_m)_{xz}]^c_{i,j-1}\Big)\cdot$$

The discretization of $\mathcal{F}^B_{i,j}$ requires the discretization of $(\sigma^B_m)_{xx}$ and $(\sigma^B_m)_{zz}$ on the p-grid and the discretization of $(\sigma^B_m)_{xz}$ on the c-grid. In the p-grid, discretization points are located on the cell centers (Fig. 3b), whereas in c-grid they are at the upper right corner of the cells (Fig. 3a). The advantage of c-grid is that the horizontal pressure gradients in the momentum equations and the flux divergence in both momentum and continuity equations are computed to the same numerical accuracy as the other terms in the momentum equations. The relation $(\sigma^B_m)_{xx} = -(\sigma^B_m)_{zz}$ follows from equation of continuity $(\partial u_m/\partial x + \partial w_m/\partial z = 0)$. So, we do not need to consider the discretization of $(\sigma^B_m)_{zz}$ explicitly. So, the discretization for $\mathcal{F}^B_{i,j}$ takes the full form as:

$$\begin{aligned}
\mathcal{F}^B_{i,j} &= \frac{\tau_c}{\delta x}\Big(\big[\nu_D\alpha_s(\Lambda_u+\Lambda_w)(D_m)_{xx}\big]^p_{i+1,j} - \big[\nu_D\alpha_s(\Lambda_u+\Lambda_w)(D_m)_{xx}\big]^p_{i,j}\Big)\\
&\quad + \frac{\tau_c}{\delta z}\Big(\big[\nu_D\alpha_s(\Lambda_u+\Lambda_w)(D_m)_{xz}\big]^c_{i,j} - \big[\nu_D\alpha_s(\Lambda_u+\Lambda_w)(D_m)_{xz}\big]^c_{i,j-1}\Big)\\
&= \frac{\tau_c}{\delta x}\Big(f_\nu(D_m)^p_2\big[(D_m)_{xx}\big]^p_{i+1,j}[\alpha_s]_{i+1,j}[\Lambda_u+\Lambda_w]_{i+1,j} - f_\nu(D_m)^p_1[\alpha_s]_{i,j}[\Lambda_u+\Lambda_w]_{i,j}\big[(D_m)_{xx}\big]^p_{i,j}\Big)\\
&\quad + \frac{\tau_c}{\delta z}\Big(\big[f_\nu(D_m)^c_2\big[(D_m)_{xz}\big]^c_{i,j}[\alpha_s]_{i,j}[\Lambda_u+\Lambda_w]_{i,j} - f_\nu(D^{u_m}_m)^c_1\big[(D_m)_{xz}\big]^c_{i,j-1}[\alpha_s]_{i,j-1}[\Lambda_u+\Lambda_w]_{i,j-1}\big]\Big)\cdot
\end{aligned} \tag{27}$$

As in Domnik and Pudasaini [13], the central differences are also applied for the discretization of $\big[(D_m)_{xx}\big]^p_{i,j}$, $\big[(D_m)_{zz}\big]^p_{i,j}$ and $\big[(D_m)_{xz}\big]^c_{i,j}$. The norm of the strain rate tensor is $\|\mathbf{D}_m\| = 2\sqrt{(D_m)^2_{xx}+(D_m)^2_{xz}}$, where normal rates are discretized on p-grid and shear rates are discretized on c-grid (Fig. 3):

$$\big[(D_m)_{xx}\big]^p_{i,j} = \frac{1}{\delta x}((u_m)_{i,j} - (u_m)_{i-1,j}),$$

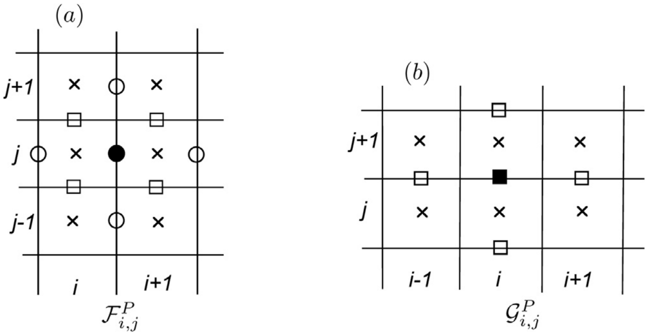

Fig. 4. Discretization of pressure-dependent terms: The filled circle and rectangle represent the discretization points of $\mathcal{F}^P_{i,j}$ and $\mathcal{G}^P_{i,j}$ respectively. Open circles represent u_m-velocities, squares represent w_m-velocities and crosses represent pressures p_m.

$$\left[(D_m)_{xz}\right]^c_{i,j} = \frac{1}{2\delta z}((u_m)_{i,j+1} - (u_m)_{i,j}) + \frac{1}{2\delta x}((w_m)_{i+1,j} - (w_m)_{i,j}),$$

$$(D_m)^p_1 = \sqrt{\left(2\left[(D_m)_{xx}\right]^p_{i,j}\right)^2 + \left(\left[(D_m)_{xz}\right]^c_{i,j} + \left[(D_m)_{xz}\right]^c_{i,j-1}\right)^2},$$

$$(D_m)^p_2 = \sqrt{\left(2\left[(D_m)_{xx}\right]^p_{i+1,j}\right)^2 + \left(\left[(D_m)_{xz}\right]^c_{i,j} + \left[(D_m)_{xz}\right]^c_{i,j-1}\right)^2},$$

$$(D_m)^c_1 = \sqrt{\left(\left[(D_m)_{xx}\right]^p_{i+1,j} + \left[(D_m)_{xx}\right]^p_{i,j}\right)^2 + \left(2\left[(D_m)_{xz}\right]^c_{i,j-1}\right)^2},$$

$$(D_m)^c_2 = \sqrt{\left(\left[(D_m)_{xx}\right]^p_{i+1,j} + \left[(D_m)_{xx}\right]^p_{i,j}\right)^2 + \left(2\left[(D_m)_{xz}\right]^c_{i,j-1}\right)^2},$$

where $(D_m)^p_1, (D_m)^p_2, (D_m)^c_1$ and $(D_m)^c_2$ are the corresponding by norms $\|\mathbf{D}_m\|$ on p- and c-grid. Similarly, $\mathcal{G}^B$ can be discretized. The values required for the discretization of $\mathcal{F}^B$ and $\mathcal{G}^B$ are shown in Fig. 3.

3.1.3. Discretization of pressure-dependent terms

The pressure dependent term, $\mathcal{F}^P$ (18) can be discretized as

$$\left[\mathcal{F}^P\right]^{u_m}_{i,j} = \left[f_0\right]^{u_m}_{i,j}\left[p_m\right]^{u_m}_{i,j} + \left[f_x\right]^{u_m}_{i,j}\left[\frac{\partial p_m}{\partial x}\right]^{u_m}_{i,j} + \left[f_z\right]^{u_m}_{i,j}\left[\frac{\partial p_m}{\partial z}\right]^{u_m}_{i,j},$$

where we propose the following discretizations for the mixture pressure and its derivatives as in Domnik and Pudasaini [13].

$$\begin{aligned}
\left[p_m\right]^{u_m}_{i,j} &= \frac{1}{2}\left[(p_m)_{i+1,j} + (p_m)_{i,j}\right],\\
\left[\frac{\partial p_m}{\partial x}\right]^{u_m}_{i,j} &= \frac{1}{\delta x}\left[(p_m)_{i+1,j} - (p_m)_{i,j}\right],\\
\left[\frac{\partial p_m}{\partial z}\right]^{u_m}_{i,j} &= \frac{1}{4\delta z}\left[(p_m)_{i+1,j+1} + (p_m)_{i,j+1} - (p_m)_{i+1,j-1} - (p_m)_{i,j-1}\right].
\end{aligned}$$

Since $\tau_c f_0 = \tau_p \mathcal{F}^B$, the discretization of f_0 is also similar to the discretization of $\mathcal{F}^B$. The other factors are discretized as [13]

$$\left[f_x\right]^{u_m}_{i,j} = \tau_p\left(\left[(D_m)_{xx}\right]^{p_m}_{i+1,j} + \left[(D_m)_{xx}\right]^{p_m}_{i,j}\right) f_v(D^{u_m}_m)[\Lambda_u + \Lambda_w]_{i,j}[\alpha_s]_{i,j},$$

$$\left[f_z\right]^{u_m}_{i,j} = \tau_p\left(\left[(D_m)_{xz}\right]^{c}_{i,j} + \left[(D_m)_{xz}\right]^{c}_{i,j-1}\right) f_v(D^{u_m}_m)[\Lambda_u + \Lambda_w]_{i,j}[\alpha_s]_{i,j},$$

where the norm of the strain rate tensor is approximated by

$$D^{u_m}_m = \sqrt{\left(\left[(D_m)_{xx}\right]^{p_m}_{i+1,j} + \left[(D_m)_{xx}\right]^{p_m}_{i,j}\right)^2 + \left(\left[(D_m)_{xz}\right]^{c}_{i,j} + \left[(D_m)_{xz}\right]^{c}_{i-1,j}\right)^2}.$$

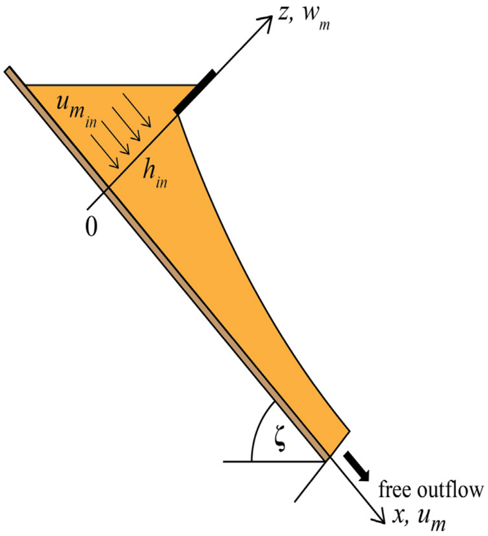

Fig. 5. Side view of the inclined chute used for the simulation of channel flow of debris material with free outflow. The debris material enters into the channel at $x = 0$ with an inlet height $h_{\mathrm{in}} = 0.15$ m and an average inlet velocity of $u_{m_{in}} = 0.9\,\mathrm{ms}^{-1}$. ζ is the inclination angle of the channel (Adopted from Domnik and Pudasaini [13]).

$\mathcal{G}^P$ can be discretized in the similar manner. The values required for the discretization of $\mathcal{F}^P$ and $\mathcal{G}^P$ are shown in Fig. 4.

3.2. Time-stepping loop

We begin with the given initial values for mixture velocities u_m and w_m at time $t = 0$. Time is increased by δt until the final time is reached. If at the nth time step, the values of the variables are known, then we compute those at $(n+1)$th time step. In the nth time step,

$$F^{(n)} = \delta t\left[\mathcal{F}^N + \mathcal{F}^B + \mathcal{F}^P\right]^{(n)}, \tag{28}$$

$$G^{(n)} = \delta t\left[\mathcal{G}^N + \mathcal{G}^B + \mathcal{G}^P\right]^{(n)}. \tag{29}$$

An Euler scheme is used for time discretization, and central differences for the discretization of the pressure gradient. F and G are discretized as proposed in Sections 3.1.1–3.1.3.

$$\begin{aligned}(u_m)_{i,j}^{(n+1)} &= (u_m)_{i,j}^{(n)} + F_{i,j}^{(n)} - \frac{\delta t}{\delta x}\left((p_m)_{i+1,j}^{(n+1)} - (p_m)_{i,j}^{(n+1)}\right),\\ (w_m)_{i,j}^{(n+1)} &= (w_m)_{i,j}^{(n)} + G_{i,j}^{(n)} - \frac{\delta t}{\delta x}\left((p_m)_{i+1,j}^{(n+1)} - (p_m)_{i,j}^{(n+1)}\right).\end{aligned} \tag{30}$$

To complete the momentum computation in time, the terms on the right hand side of (30) must also be associated with a time level. F and G are evaluated at the time level n, i.e., all velocities in (28)–(29) belong to the time level n, where as $\partial p_m/\partial x$, and $\partial p_m/\partial z$ are associated with the time level $n+1$. Thus, the momentum equations for the mixture in x- and z-directions are fully discretized in time and space. The pressure-Poisson equation for p_m is discretized by using the central difference scheme:

$$\begin{aligned}&\frac{(p_m)_{i+1,j}^{(n+1)} - 2(p_m)_{i,j}^{(n+1)} + (p_m)_{i-1,j}^{(n+1)}}{\delta x^2} + \frac{(p_m)_{i,j+1}^{(n+1)} - 2(p_m)_{i,j}^{(n+1)} + (p_m)_{i,j-1}^{(n+1)}}{\delta z^2}\\ &\quad = \frac{1}{\delta t}\left[\frac{(F)_{i,j}^{(n)} - (F)_{i-1,j}^{(n)}}{\delta x} + \frac{(G)_{i,j}^{(n)} - (G)_{i,j-1}^{(n)}}{\delta z}\right].\end{aligned} \tag{31}$$

Although, the computational tools and discretization techniques of the model here are similar in the form to those in Domnik and Pudasaini [13], we face more challenges because of the presence of the generalized bulk viscosity, velocity and pressure, and due to the fact that the discretization has been presented for more general mixture flows that include inertial and dynamical coefficients.

3.3. Pressure calculation for a pressure-dependent basal slip

Following Domnik and Pudasaini [13], Domnik et al. [14], and von Boetticher et al. [73], we employ Coulomb sliding law to compute the bottom boundary velocity $(u_m)_{i,j-1}$ for the cell $\mathrm{C}_{i,j}$. The following discretization is used at the lower right corner of the cell $\mathrm{C}_{i,j}$ adjacent to the boundary cell $\mathrm{C}_{i,j-1}$:

$$
\begin{aligned}
c^F &= \begin{cases} \dfrac{(u_m)_{i,j}}{|(\mathbf{u}_m)_{i,j}|}\tan\delta, & (u_m)_{i,j} \neq 0, \\ 0, & (u_m)_{i,j} = 0, \end{cases} \qquad (32)\\
p_m^b &= \frac{1}{2}[(p_m)_{i,j} + (p_m)_{i+1,j}],
\end{aligned}
$$

$$
\begin{aligned}
\left[\frac{\partial u_m}{\partial z}\right]^b &= \frac{1}{\delta z}\left((u_m)_{i,j} - (u_m^b)_{i,j-1}\right), \\
\left[\frac{\partial u_m}{\partial x}\right]^b &= \frac{1}{4\delta x}\left((u_m^b)_{i+1,j} + (u_m^b)_{i+1,j-1} - (u_m)_{i-1,j} - (u_m^b)_{i-1,j-1}\right). \qquad (33)
\end{aligned}
$$

Following Domnik and Pudasaini [13], c^F is discretized at $z = \delta z/2$ rather than at the bottom ($z = 0$), assuming that the sign of the tangential velocity does not change within a half cell height. The pressure at the bottom, p_m^b is approximated with the help of the next available pressure values. Central differences are used for $\left[\frac{\partial u_m}{\partial z}\right]^b$, and an additional averaging is done for $\left[\frac{\partial u_m}{\partial x}\right]^b$ as shown in (33). The pressure and rate-dependent Coulomb-viscoplastic mixture rheology (21), can be expressed in terms of the bottom boundary (slip) velocities $(u_m^b)_{i,j}$:

$$
(u_m^b)_{i,j-1} + c^{u_m}_{i,j}\left((u_m^b)_{i+1,j-1} - (u_m^b)_{i-1,j-1}\right) = (u_m)_{i,j} - c^{u_m}_{i,j}\left((u_m)_{i+1,j} - (u_m)_{i-1,j}\right) - c^{p_m}_{i,j}[(p_m)_{i,j} + (p_m)_{i+1,j}], \qquad (34)
$$

where $c^{u_m}_{i,j} = \dfrac{c^F_{i,j}}{2}\dfrac{\delta z}{\delta x}$, $c^{p_m}_{i,j} = \dfrac{\delta z}{2}\dfrac{c^F_{i,j}}{[\Lambda_{\eta_m}]^b_{i,j}}$.

Equation (34) can be written as a system of N_c linear equations:

$$
A\mathbf{u}_m^b = \mathbf{b}_c - B\mathbf{p}_m, \qquad (35)
$$

with $A \in \mathbb{R}^{N_c \times N_c}$, $B \in \mathbb{R}^{N_c \times N_I}$, b_c and $u_m^b \in \mathbb{R}^{N_c}$, where N_c is given by the number of Coulomb cells.

4. Simulation results

4.1. Simulation set-up and parameters

The simulation channel is 1 m long, has an inclination of $\zeta = 45°$ and the debris mixture of different compositions is continuously fed from a silo. The inlet height is $h_{\mathrm{in}} = 0.15$ m and the mean inlet velocity is $u_{m_{\mathrm{in}}} = 0.9\ \mathrm{ms}^{-1}$. The flow configuration used in the simulations is similar to Pudasaini et al. [59], and Domnik and Pudasaini [13]. In our simulations, we use kinematic viscosity for solid $\nu_s = 0.3591\ \mathrm{m}^2\mathrm{s}^{-1}$, and for fluid $\nu_f = 10^{-3}\ \mathrm{m}^2\mathrm{s}^{-1}$, Bingham exponent factor $m_y = 10$, pressure dependent yield stress parameter $\tau_p = \sin\phi = 0.5446$, cohesion $\tau_c = 60$ Pa (bed friction angle $\delta = 25°$, internal friction angle of the solid grains, $\phi = 33°$). For the sake of simplicity, we set the velocity and pressure drifts close to unity, i.e., $\lambda_u, \lambda_w, \lambda_p \approx 1$ so that the inertial and dynamical coefficients are close to unity and the viscosities Λ_{η_u} and Λ_{η_w} reduce to $\Lambda_m = \nu_s^e\alpha_s + \nu_f\alpha_f$. The simulation results are mainly presented for the time evolution of the full two-dimensional velocity and pressure fields for varying solid volume fractions.

Next, we justify the reason for taking different solid volume fractions in the mixture. One of the major aspects of the model (1)–(3) is the mixture viscosity, Λ_{η_m} (in reduced form, $\Lambda_m = \nu_s^e\alpha_s + \nu_f\alpha_f$), as a combination of the effective solid and the fluid viscosities in the mixture which is achieved via the solid (and, fluid) volume fraction. The non-linear mechanics inherited in the complex generalized mixture viscosity controls the flow velocities and pressure and thus the flow field pattern. Therefore, it is of fundamental interest to analyze the model performance and its dynamics with respect to the changing volume fraction of the solid in the mixture. Since we are interested in the mechanically stronger frictional debris material, we mainly consider debris mixtures in which the solid volume fraction plays a major to dominant role i.e., the mixture flows which are slightly dilute (say, $\alpha_s = 0.35$) to very dense (say, $\alpha_s = 0.75$), and almost dry (say, $\alpha_s = 1.00$). All these are possible scenarios in natural (potentially also in industrial) flows. Another important aspect in considering the flow with different α_s values is that the flow dynamics and the final deposition morphology are observed to be substantially to strongly affected by the initial material compositions [11,57]. One way to define such a composition is by considering the different fractions of the solid in the mixture at the time of release.

In what follows, in-depth analyses are presented for the field variables (velocities and pressure) and other dynamical quantities namely, the mixture viscosity and the full dynamic pressure. These results highlight the mechanical insight of the recently constructed generalized quasi two-phase mass flow model (1)–(3), and hence pave the way for further more complex simulations with potential applications.

4.2. *Velocity*

Perhaps the most important dynamical aspect of the simulation is the time dependence of the flow which we examine first. This is important in describing the overall flow dynamics and the temporal and spatial variations of the flow depth and the velocity distributions along the flow depth. Here, we investigate the complete flow evolution from the silo gate (flow release) down the entire channel. The results are presented in Figs. 6–8 for the solid volume fractions $\alpha_s = 0.35, 0.75, 1.00$, respectively.

We start the analysis with the more dilute flow ($\alpha_s = 0.35$) in Fig. 6, which shows the simulated flow depth (in background gray) and velocity vectors throughout the channel. For early times (panels (a)–(c)), due to the large pressure gradients, the maximum velocity is located at the front head, somewhere between the free surface and the channel bottom. For later times (panels (d)–(f)), the vertical position of the maximum velocity is marching closer to the free surface and towards the forehead. So, it shows the evolution of the maximum velocity region within the sliding and dynamically evolving debris material. As time elapses, the flow front slowly develops into a thick (surge-type) structure, which is a bit different than in Domnik and Pudasaini [13] for granular flows but, seems to corroborate with observed phenomena of surging heads in debris flows. Furthermore, in time, and further downslope (panels (c)–(f)), the (xz-) shearing of the velocity field becomes more apparent. These results are in line with our physical intuition and some observed phenomena [4,6,11,15,30,31,34].

Figure 10 plots the shear rate profile $\dot{\gamma}$ with the channel downslope distance (x-direction) and the maximum flow depth in z-direction for $\alpha_s = 0.35$. It shows the variation of the tangential velocity of the mixture u_m with the flow normal direction, z. The simulation produces a clear and strong shear profile through a substantial flow depth in the vicinity of the bottom with a non-zero slip velocity at the bottom. The shear rate increases along the downslope channel position. However, it decreases in the upper region of the flow, and is close to zero in the vicinity of the free surface, but, as in Domnik and Pudasaini [13], it is even appears negative at the surface near the silo inlet. This is compatible with the tractionless free-surface condition. With the no-slip condition on the bottom, the velocity would be zero at the bottom [see, e.g., 13,14]. This means that the appropriate choice of the bottom boundary condition is important to correctly control and describe the flow dynamics in rapid debris mixture flows in steep channels. Experiments in rapid granular and debris flows in inclined channels show that the material slips along the channel (so, the no-slip bottom boundary condition is physically inappropriate) and shears mainly in the vicinity of the bottom, whereas the shear-rate adjacent to the free-surface is low [40,59,64]. These typical characteristics of rapid debris flows are illustrated in Fig. 6.

We continue with the analysis for the higher values of the solid volume fractions, $\alpha_s = 0.75, 1.00$, in Figs. 7 and 8, respectively which, as above, show the simulated flow depth (in background gray) and the corresponding velocity vectors in color maps. At a first glance, Figs. 6–8 look similar to each other. However, there are substantial differences between the corresponding panels in these figures, both qualitatively and quantitatively. As these figures

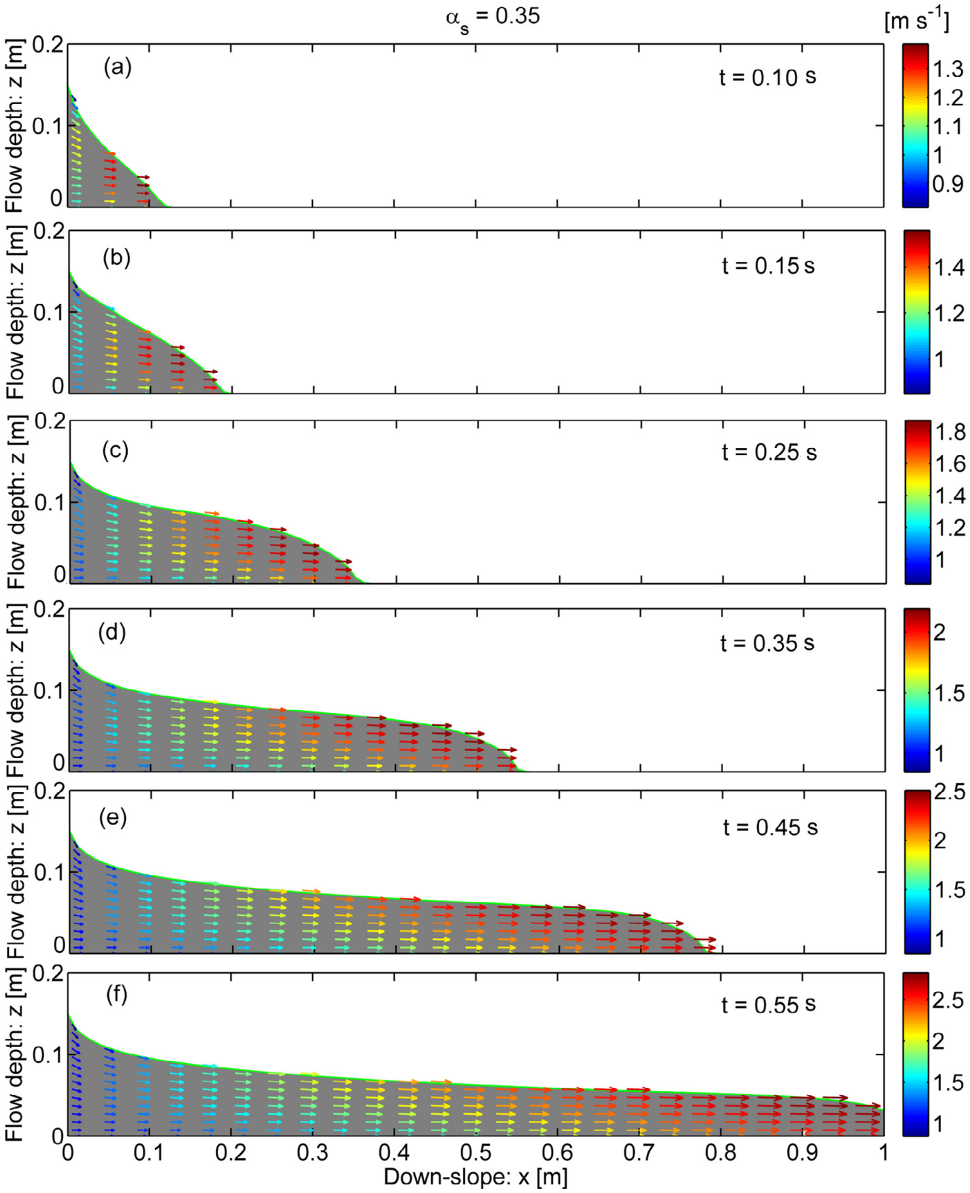

Fig. 6. The full two dimensional mixture velocity vectors along the channel for the solid volume fraction $\alpha_s = 0.35$. The background gray map indicates the geometries and color arrows indicate the velocity vectors of the evolving debris mixture as it moves down an inclined channel.

are produced by increasing the solid volume fractions, the material becomes mechanically stronger from one figure to another. These are characterized by (i) the front position (or, the travel distance), essentially measuring the mobility of the flow, (ii) the flow velocity (or, the kinetic energy of the flow), (iii) the geometric evolution of the front and the main body of the flow (the overall flow evolution). Below, we analyze all three aspects associated with flow mechanics and their nonlinearity in detail.

4.2.1. The front position

The accurate knowledge of the front position of the flow is very important in the dynamic simulation as it is the indicator of the flow mobility [42,60]. The flow front in the final panel (f), in Fig. 6 has already exited the

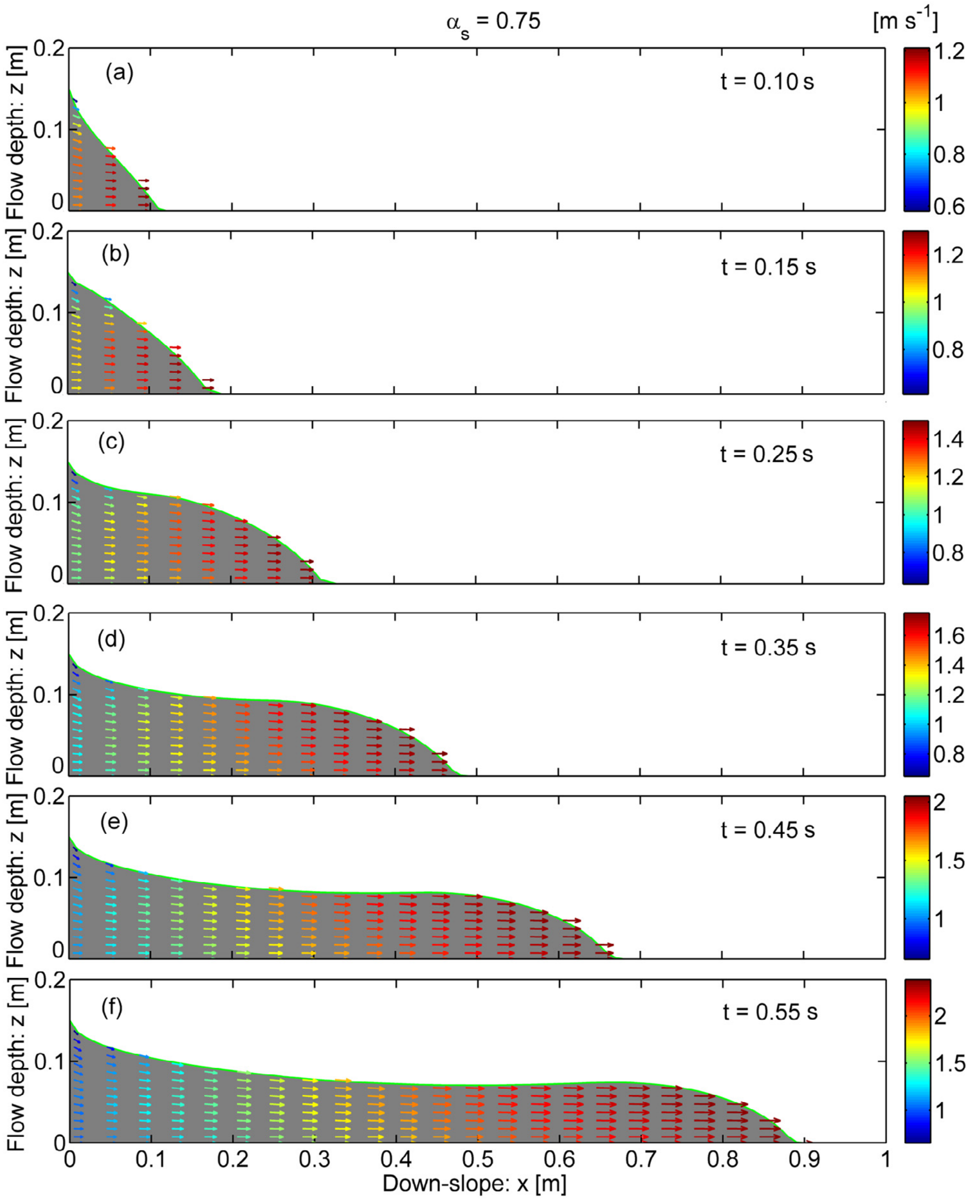

Fig. 7. The full two dimensional mixture velocity vectors along the channel for the solid volume fraction $\alpha_s = 0.75$. The background gray map indicates the geometries and color arrows indicate the velocity vectors of the evolving debris mixture as it moves down an inclined channel. At later times, the flow moves less farther downslope with decreased maximum velocity than in Fig. 6.

lower end of the computational domain (i.e., $x = 1$ m, the channel outlet), whereas the front positions for other simulations ($\alpha_s = 0.75, 1.00$, respectively, for Fig. 7, Fig. 8) are only (approximately) at (0.88, 0.82)m. This shows that the initial mixture with lower solid volume fraction travels farther downslope as compared to the initial mixture with higher solid fraction. As the effective mixture viscosity increases with increasing solid fraction, this can be explained in connection to the material strength that reduces the deformation, and thus the flow and travel distance. This fact will be clarified more in Section 4.4 and Fig. 14. The flow fronts are nearly at the same downslope positions for the early times. However, the flow fronts for different α_s differ substantially as time progresses. The position of the flow fronts for individual α_s and the change of positions for all three α_s show non-linear behavior. Moreover, as compared to the small scale simulations, these changes in the flow front positions are substantial,

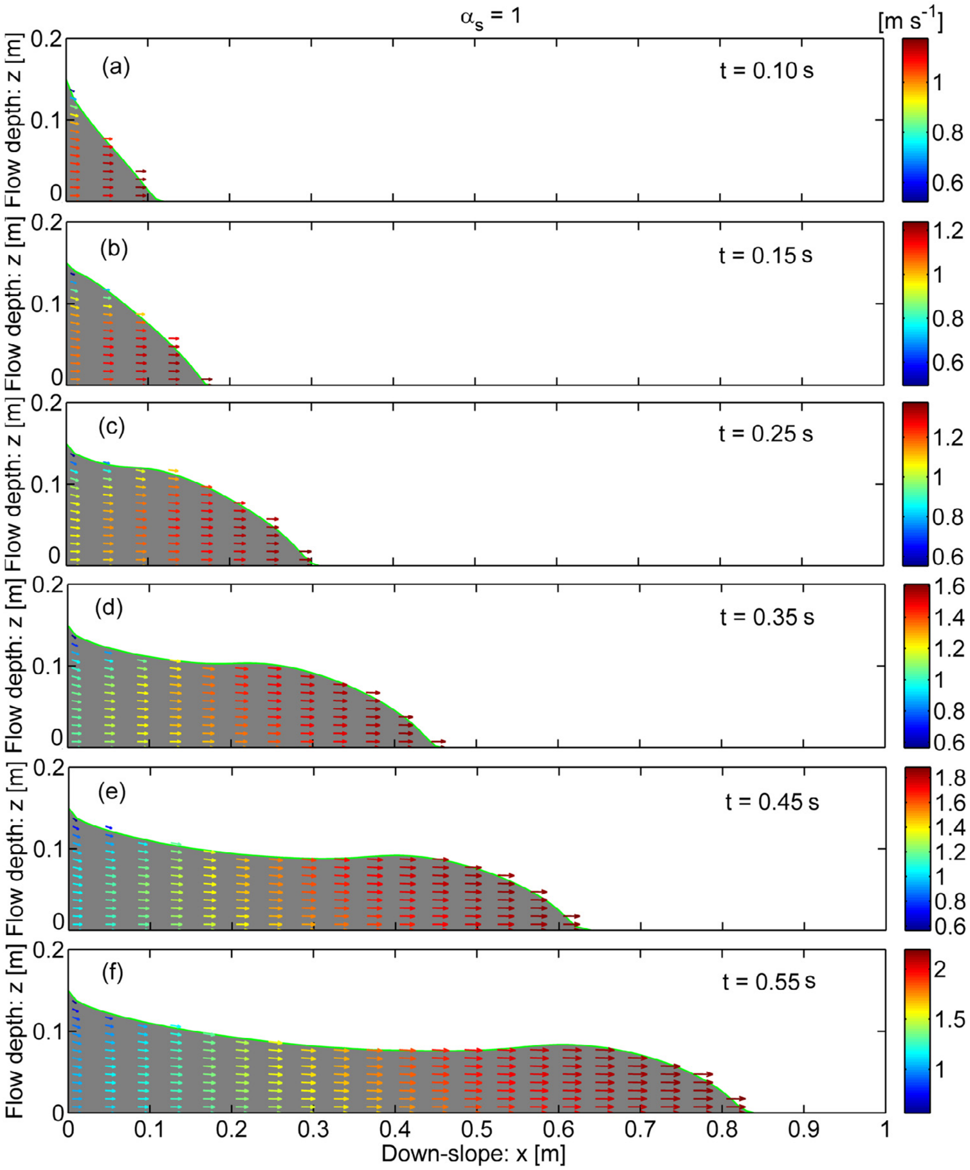

Fig. 8. The full two dimensional mixture velocity vectors along the channel for solid volume fraction $\alpha_s = 1$. The background gray map indicates the geometries and color arrows indicate the velocity vectors of the evolving debris mixture as it moves down an inclined channel. The front moves even less farther downslope and has lower velocity than the previous case.

because when upscaled to the real flow situations in which the flows travel several tens (sometimes even hundreds of) Km [44–46], the difference could be on the order of Km. That would be rather big numbers for the hazard mitigation, planning, and public safety.

4.2.2. The flow velocity

Flow velocity is the key in the entire dynamic simulation as most of the dynamical variables are induced from velocity. Moreover, pressure and the velocity are the only field variables on which the model is developed. The flow depth, the Froude number, shear-rate, impact pressures, kinetic energy, etc. are other induced quantities. So, we need to carefully analyze the velocity fields. As a reference, we only compare the maximum velocity for the last panels (i.e., for the time $t = 0.55$ s) in Figs. 6–8. The maximum velocities for Fig. 6 ($\alpha_s = 0.35$), Fig. 7

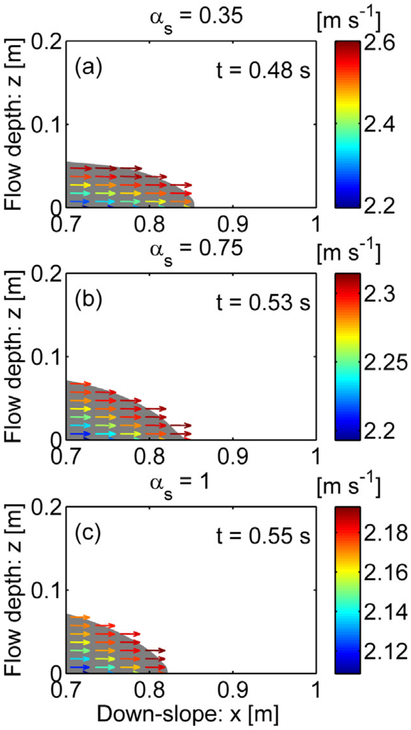

Fig. 9. Comparison of velocity field for the debris head that occurs at the region $0.7 \leq x \leq 0.85$ m.

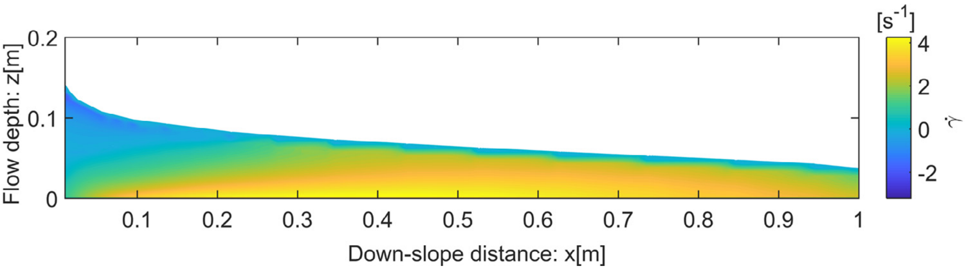

Fig. 10. The shear rate $\dot{\gamma} = \partial u_m/\partial z$ (gradient of the tangential velocity in normal direction to the bottom surface of the channel) for different channel positions. $\dot{\gamma}$ is maximum at the bottom and gradually decreases to the free surface.

($\alpha_s = 0.75$) and Fig. 8 ($\alpha_s = 1.00$) are about 2.6, 2.25 and 2.1 m s^{-1}, respectively. Figure 9 plots the velocity fields of the debris mixture flow for the region $0.7 \leq x \leq 0.85$ m corresponding to Figs. 6–8, where the frontal debris head is at $x = 0.85$ m. The velocity of the debris head is nearly 2.6 m s^{-1} for $\alpha_s = 0.35$ at $t = 0.48$ s, 2.31 m s^{-1} for $\alpha_s = 0.75$ at $t = 0.53$ s and 2.19 m s^{-1} for $\alpha_s = 1$ at $t = 0.55$ s. The maximum velocity of the debris head is highest for $\alpha_s = 0.35$ although it occurs at earlier time stage than for higher α_s. The differences in these maximum velocities are considerable and indicate nonlinearity even for these small scale simulations, showing that it can be on the order of 20%. Thus, the difference in these numbers can be very important in large scale natural flows, and it plays a substantial role in appropriately designing the defense structures as these structure are constructed with the requirements of withstanding the impact pressures that is technically proportional to the square of the velocity. However, flow-structure-interactions and computation of impact pressure of the flow on structures can be found in Kattel et al. [37] for two-phase flows. Furthermore, a closure look at the velocity fields (in each corresponding panel of different figures) reveals that for higher values of α_s, the vertical shearing (mainly in the vicinity of the channel bottom) decreases. That is, the xz-shearing is more pronounced in the material containing less solid particles. This is physically relevant as the higher amount of the solid particles in the mixture makes the flow more frictional and more viscous as compared to the lower amount of solid. Thus, the higher amount of fluid effectively brings the mixture closer to the more viscous material akin to a usual fluid. Such a strong mechanical response of the material has been revealed here with the new complex mixture viscosity.

4.2.3. The geometric evolution

The flow height and the inundation area are the most often considered dynamical variables in the mass flow simulations [3,5,10,11,30,52,60,63,70]. The reason is clear, as in most of the natural events, the flow velocity measurements are either very limited, or not possible at all due to the extreme nature of the flow and also mainly the unknown timing, magnitude and complexity of the flow. However, the flow coverage area (inundation area), and the depth in the deposition, can be measured or, estimated even ages after the event took place [44,45]. For this reason, information of the flow depth evolution is important. This information is needed for the computation of the impact force. A close scrutiny between the figures shows three interesting and technically important features: (i) The flow becomes thicker and the flow depth is increasing from Fig. 6 to Fig. 8 as the α_s values increase. This can be explained simply from the mass balance, because as flow slows down due to mechanically strong material, it deforms less, resulting in the higher flow depth. (ii) The front head develops into bulking, akin to the surge development in debris flows [4,6,11,15,30,31,34]. The reason for this is the increase in the solid fraction results in the increase of the effective viscosity that slows down the motion of the flow front, while at the same time the downslope material flux continues. Consequently, the front begins slowly to bulk (due to the increased material strength against the applied gravity and shear loads). This is clearly seen in Figs. 7 and 8, but almost not appearing in Fig. 6. (iii) The main body shows depletion. Such depletion begins to develop from the early stage, already at $t = 0.25$ s in Fig. 8, that in later time, amplifies and stretches along the channel behind the flow head. This can also be explained, because in the back, the flow is relatively stretching, but in the front there is a strong mechanical resistance, forcing to result into a depletion in the flow body. Such a change in the flow geometry is important as it determines the hydrograph, and thus the impact pressures of the flow.

4.3. Pressure

The pressure fields are presented in Figs. 11–13. They exhibit layered structures along the channel, which originate both from the depth-dependence of the pressure and the flow dynamics. The pressure first increases along the x-direction, due to the considerable fall in flow depth, which develops along with a compressional state of the material near the silo inlet. Later on, the pressure decreases along the channel, because the gravitational acceleration causes a dispersional (spreading) downslope motion. It is important to note that the pressures here are the full dynamic pressures in contrast to the usual hydrostatic pressure often dealt with in granular flows and mixture mass flows, such as avalanches and debris flows [12,53,54,58]. The full dynamic pressure p can be expressed as a sum of the hydrostatic (p_H) and the dynamic (p_D) pressure: $p = p_H + p_D$, where $p_H = \rho_m g \cos\zeta(h - z)$ with the flow height h. Figs. 11–13 indicate that the dynamic pressure is important in debris flows. Due to the extensional motion of the mixture material in the channel, the hydrostatic pressure significantly (not shown here explicitly, but can be derived easily from the results presented here) underestimates the full pressure p. This becomes dominant near the silo inlet. However, the dynamic pressure is not uniform through the flow depth even far away from the silo inlet. As in Domnik and Pudasaini [13] and Domnik et al. [14], analysis of such phenomena is made possible with the full dimensional consideration of the flow. As in the velocity fields, the solid volume fraction substantially influences the pressure fields. Close to the silo inlet, the pressure distribution looks similar for all α_s considered. However, as α_s increases, the pressure fields become more and more non-linear in the far downstream, see Figs. 12 and 13. Further interesting observation is that due to the bulking around the flow head and depletion behind the surge, the layered pressure fields are strongly curved. Importantly, as α_s increases, pressure maxima develop around the flow head. This information is crucial in calculating dynamic pressure at defense structure [37].

As mass moves along the slope, the dynamic pressure becomes more and more important. Thus, the hydrostatic pressure along the channel cannot appropriately describe the pressure distribution. For a long travel distance the hydrostatic pressure may be negligible (due to the thinning of the flow) but the dynamic pressure may largely dominate the full pressure distribution.

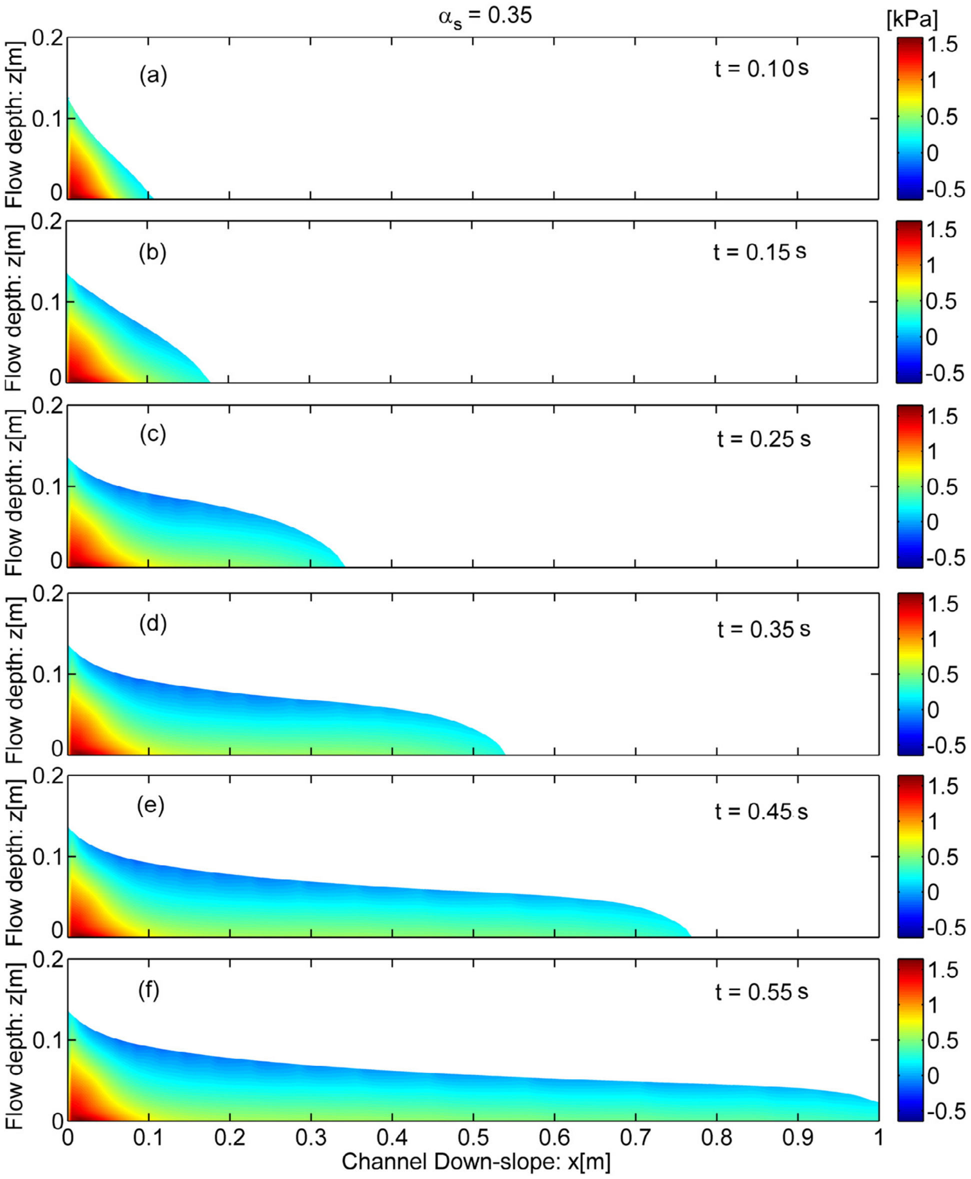

Fig. 11. Time evolution of the full dynamic pressure fields along the channel for solid volume fraction $\alpha_s = 0.35$. The layered structures along the channel originate both from the depth-dependence of the pressure and the flow dynamics as it moves down an inclined channel.

4.4. The mixture viscosity

The above results and discussions clearly show the importance of the effective mixture viscosity in the dynamics of the flow via the solid volume fraction, α_s, and the strain-rate. So, here, we analyze how the effective mixture viscosity (Λ_{η_m}) evolves as a function of the solid volume fraction and strain-rate. First, we deal with Λ_{η_m} as a function of α_s. The mixture viscosity depends directly on α_s and indirectly on the drift factor, λ_u. Explicit form of λ_u is not yet known, and requires further research. However, λ_u as a decreasing function of α_s is a legitimate choice, because, as α_s increases the decreasing fluid velocity is a reasonable scenario. To begin with, without loss of generality, here we assume a simple functional relation for λ_u as:

$$\lambda_u = \xi / \left(\chi + (\alpha_s/\alpha_{sm})\right)^n , \qquad (36)$$

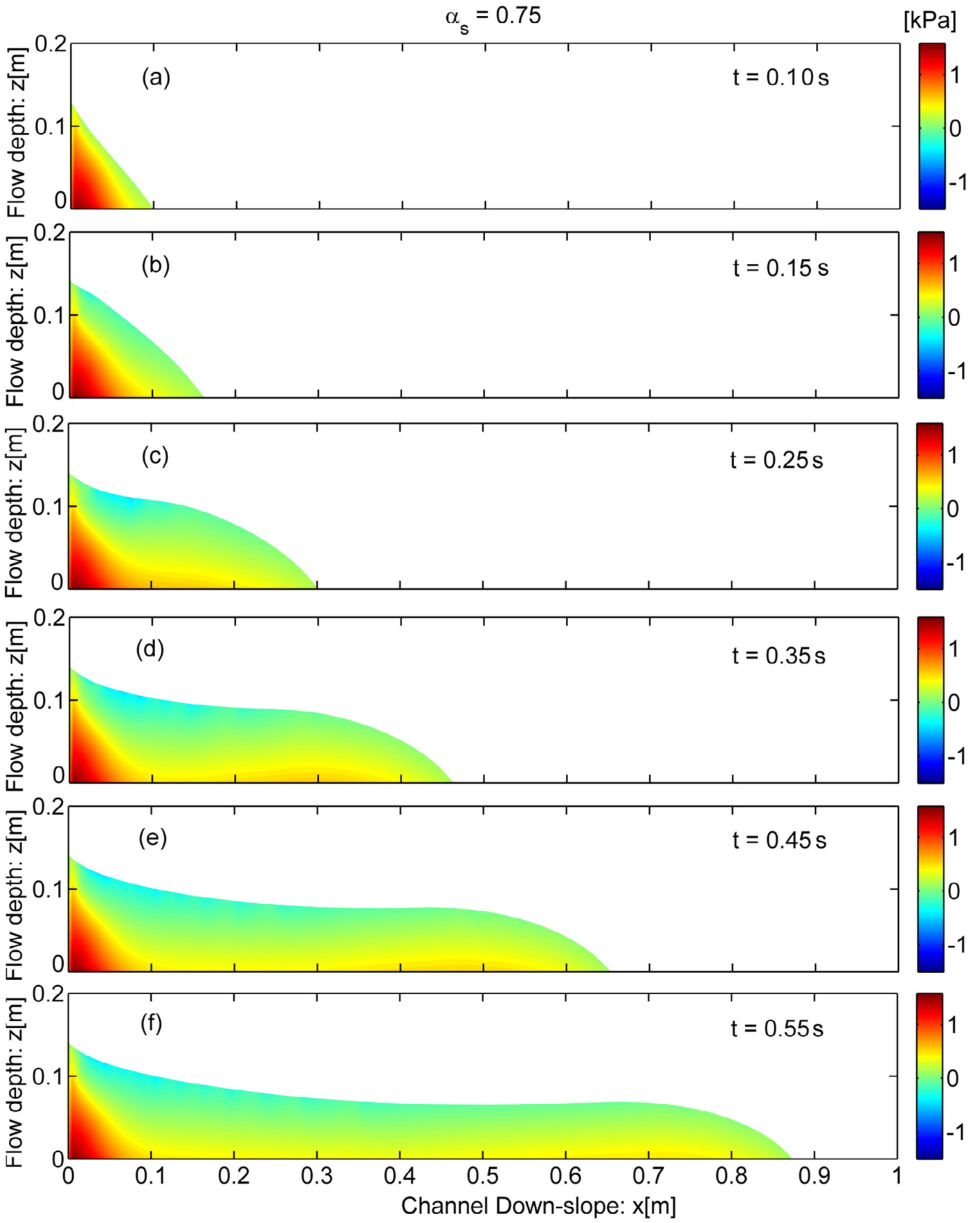

Fig. 12. Time evolution of the full dynamic pressure fields along the channel for solid volume fraction $\alpha_s = 0.75$. The layered structures along the channel originate both from the depth-dependence of the pressure and the flow dynamics as it moves down an inclined channel.

where, the parameters ξ, χ and n determine the form and magnitude of λ_u, and α_{sm} is the maximum packing of the solid particles, which describes the physical-state of the mixture, so does the viscosity of the solid and fluid phases. If x- and z-directional velocity drifts are identical, i.e., $\lambda_u \approx \lambda_w$, then mixture viscosity Λ_{η_m} in (8) becomes

$$\Lambda_{\eta_m} \approx (\nu_s^e \alpha_s + \nu_f \alpha_f \lambda_u)\Lambda_u. \tag{37}$$

Inserting (36) in (37) provides a close functional form for the mixture viscosity.

Figure 14 plots the scaled mixture viscosity, Λ_{η_m}/ν_f against the scaled solid volume fraction, α_s/α_{sm}. The values of the kinematic viscosities appearing in (37) are chosen as $\nu_s = 0.3591\ \mathrm{m^2s^{-1}}$ and $\nu_f = 10^{-3}\ \mathrm{m^2s^{-1}}$, respectively. The value of α_{sm} ranges from 0.5 to 0.75 [28]. Here, we have chosen $\alpha_{sm} = 0.65$. For numerical purpose, other

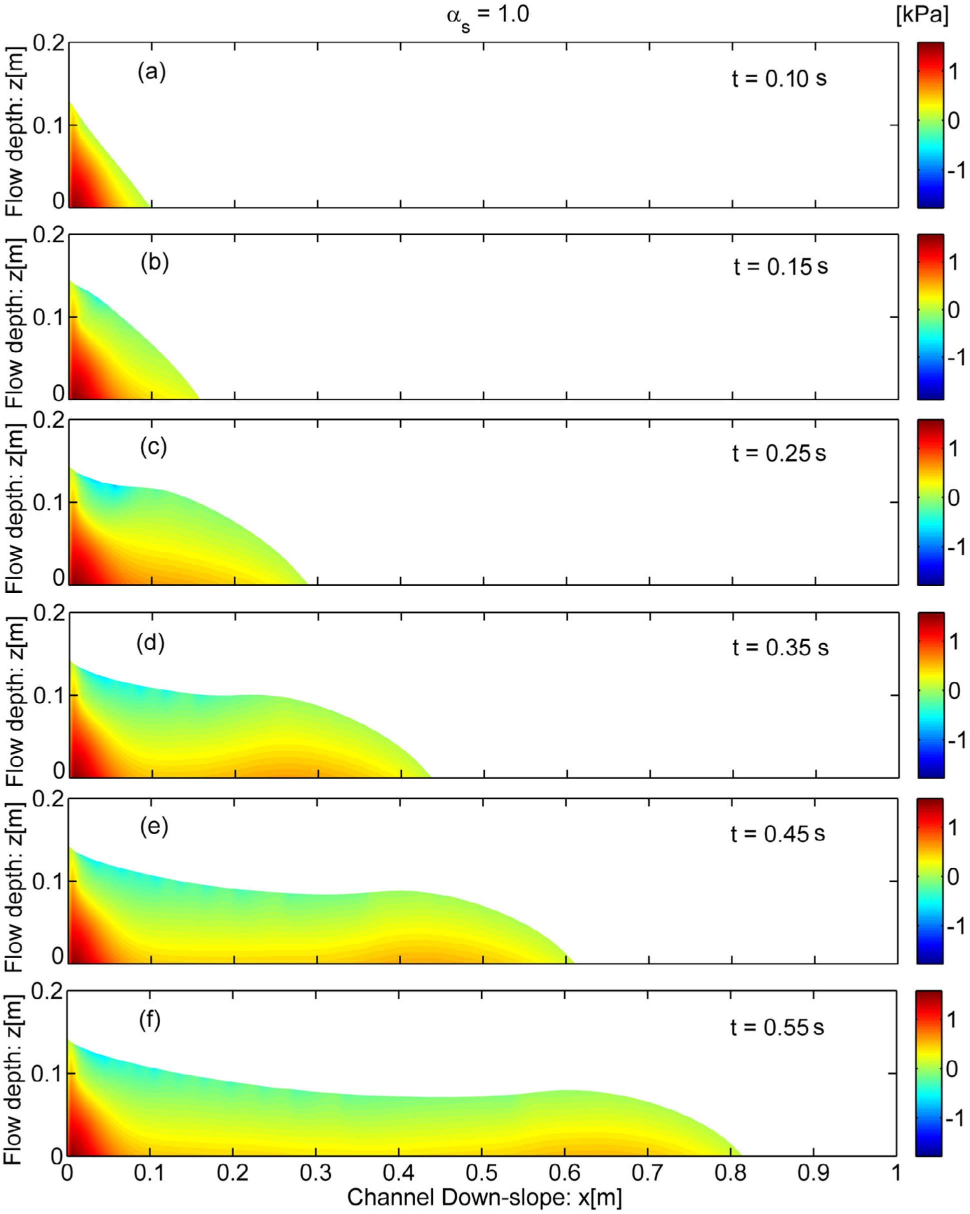

Fig. 13. Time evolution of the full dynamic pressure fields along the channel for solid volume fraction $\alpha_s = 1.0$. The layered structures along the channel originate both from the depth-dependence of the pressure and the flow dynamics as it moves down an inclined channel.

parameters are taken as $(\xi, \chi, n) = (0.1, 0.0005, 4.0)$. We have considered the solid and fluid densities, $\rho_s = 2700$ kg m^{-3} and $\rho_f = 1000$ kg m^{-3} respectively, and so the bulk mixture density, ρ_m changes according to the solid volume fraction, α_s during the flow. In the present numerical simulation, we have taken the yield stress of 60 Pa [13]. These chosen parameter values are subjected to change depending on the material composition and other flow situations. The figure reveals a very interesting, potentially important, behavior of the mixture viscosity. Moreover, the viscosity in Fig. 14 is qualitatively similar to the mixture viscosity presented in Ishii [28], and the references therein, which deal with experimental data. However, the viscosity presented here shows highly non-linear behavior with α_s than those observed previously. The viscosity increases with α_s, but with different rates. We mention that to compare the new result with the models in Ishii [28], and also due to the nature of the mixture viscosity with

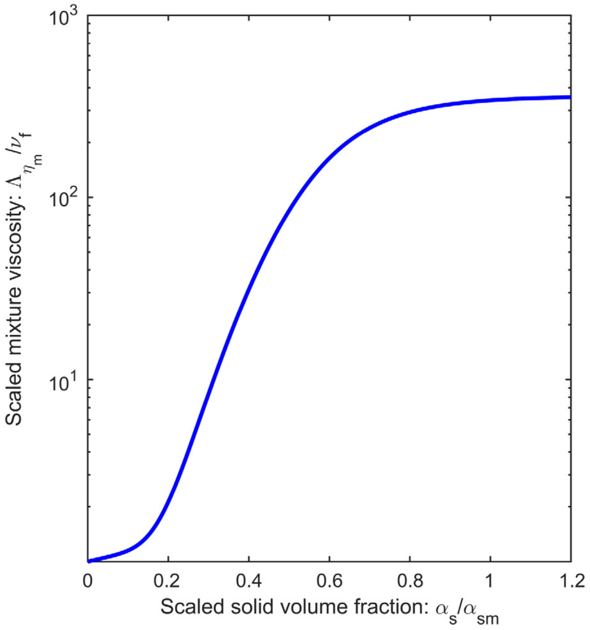

Fig. 14. The evolution of the scaled mixture viscosity as function of the scaled solid volume fraction, showing a highly non-linear complex mechanical behavior.

the solid fraction, the figure is presented in log-normal scale. The figure shows three distinct regimes: (i) For small values of the solid volume fraction, for about $\alpha_s/\alpha_{sm} \leq 0.2$, viscosity increases very slowly. This is reasonable because, for very small solid fraction, the effect of the solid particles in the mixture is negligible as the particle collision is very low and the mean free path is very large, and thus, the mixture effectively behaves as a fluid, also called macroviscous flow [2,56]. (ii) The viscosity increases rapidly in the domain $0.2 < \alpha_s/\alpha_{sm} < 0.6$. This means that this is the most probable range of the particle concentration for which the intensity of the viscosity increases rapidly. This is so because, now the material tends to respond as if it was a solid-type material so that the viscosity must quickly attain its higher limit of solid-type viscosity. (iii) However, as it enters the domain of very high solid concentration, $\alpha_s/\alpha_{sm} \geq 0.6$, the viscosity increases very slowly, and tends to saturate for further higher values of the solid volume fraction. This is also reasonable, because, the viscosity cannot always increase for further increasing value of the solid volume fraction as the material cannot be mechanically stronger than the solid-type mixture. So, all the three regimes of the mixture viscosity could be explained (or, justified) from a mechanical perspective. Although it must be tested with field or laboratory data, which is not within the scope here, these behaviors could represent the realistic, but quite complex mechanics associated with the viscosity of particle–fluid mixture flow. Such a very special behavior of the mixture viscosity as presented here is novel.

Second, we investigate how the mixture viscosity changes with the shear-rate. The results in Fig. 15 show that for large shear-rates (say, typically larger than 3 s^{-1}), Λ_{η_m} is very small. However, as the shear-rate decreases, the value of the effective mixture viscosity increases exponentially. Furthermore, the Λ_{η_m} values are higher for higher α_s values for the reasons explained above.

5. Discussion and summary

Here, we considered a novel generalized quasi two-phase bulk mixture model for mass flow down a channel [55]. The model consists of a set of highly non-linear partial differential equations for three unknowns, namely, the mixture velocities in x- and z-directions, and pressure, and are well written in conservative form to describe the complex motion of mixture of viscous fluid and granular particles. The new model has been compared with other alternative models existing in the literature, including von Boetticher et al. [73]. In structure, the considered system is very much similar to the one developed by Domnik and Pudasaini [13]. However, there are several advantages of the new model over the existing models: (i) The present model is much more advanced, captures more

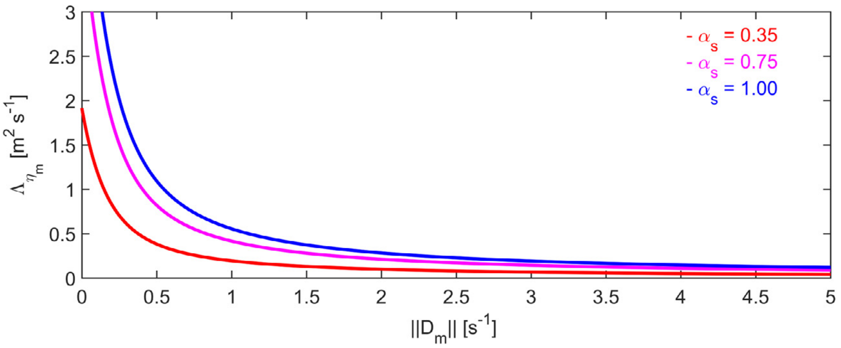

Fig. 15. Dependency of the mixture viscosity Λ_{η_m} on the strain rate for different solid volume fractions at time $t = 0.45$ s.

complex behaviors and covers the much wider spectrum than the existing mixture models. (ii) From a numerical and simulation point of view, the computational cost of the new model is reduced drastically as compared to the two-phase model. (iii) Importantly, once the mixture velocities and pressure are obtained, the two-phase dynamics of solid and fluid can be reconstructed from the drift relationships and the bulk mixture velocities, and the pressure.

In order to highlight the non-linear mechanics of the generalized quasi two-phase mixture model, with benchmark simulations, here we have mainly presented some essential aspects associated with the complex dynamics of the geometric deformation, velocity and pressure fields. This includes the detailed analyses of the full two-dimensional time evolution of these fields.

With the generalized mixture viscosity, velocity and pressure, we presented a full discretization of the model, including the inertial and dynamical coefficients appearing in the new model equations. The numerical treatment is based on the finite volume scheme that is beneficial for rapid flows and large deformations [13,17]. The computational domain is discretized using a staggered grid that prevents possible pressure oscillations. The Newtonian, Bingham and pressure-dependent terms, and the pressure-Poisson equation are discretized separately and suitably with higher order central differences. Possible instabilities are avoided by using a mixture of central difference and donor-cell discretization. The discretization and computational techniques are similar in the form to those in Domnik and Pudasaini [13]. However, complexities arise due to the generalized bulk viscosity, velocity and pressure, and effective bulk friction, and that the discretization has been presented for more general mixture flows that include inertial and dynamical coefficients. This paves the way to further expand the computational scheme and code to the extended quasi two-phase mass flow model [41] that includes even more physical aspects, namely, the virtual mass force, generalized drag and non-Newtonian viscous stress.

We have shown that it is of fundamental importance to analyze the model performance and flow dynamics with respect to the changing volume fraction of solid in the mixture — from dilute to very dense flows. Our results indicate that the highly nonlinear flow dynamics are strongly controlled by the initial material composition. With increased solid volume fractions, the material becomes mechanically stronger, and shearing decreases. These are characterized by the flow mobility and thus the kinetic energy, and the overall geometric evolution. The dynamics of the flow front positions, velocity and flow depths are substantially controlled by the material composition. These quantities play important role in appropriately designing the defense structures as these structure are constructed with the requirements of withstanding the impact pressures that is technically proportional to the square of the velocity and linearly to the flow depth and mixture density [16,18,37]. The analysis shows that proper knowledge of the initial material composition is essential for the accurate estimation of the impact pressure and the flow-obstacle-interactions. So, these are important information for the hazard mitigation, planning, and public safety.

Our results show that the maximum velocity region evolves within the sliding debris body. The flow front slowly develops into a surge-type structure. In time, and further downslope, velocity shearing becomes apparent. A strong shear profile develops through the flow depth mainly in the vicinity of the bottom, which increases along the downslope channel position. The shear rate decreases and approaches zero in the vicinity of the free surface. So, the appropriate choice of the bottom boundary condition is important to correctly describe the flow dynamics in rapid debris mixture flows in steep channels. The surface and bottom velocities behave fundamentally differently.

Simulations provide important information about the non-zero slip velocity at the channel bottom. The results show that the slip velocity increases along the slope and generally attains higher values for lower solid fraction.

In contrast to the usual hydrostatic pressure, the full dynamic pressure exhibits strongly non-linear structures along the channel. The dynamic pressure is not uniform through the flow depth. For higher solid fraction, pressure maxima develop around the flow head. It appears that the dynamic pressure can be more important than the total pressure in debris flows, and the often considered hydrostatic pressure may significantly underestimate the full pressure.

Several other technically important features are observed: The flow becomes thicker as solid fraction increases. The front head develops into bulking. The main body shows depletion. These geometric information are important as they determine the flow hydrograph, and consequently the impact force. The novel result for mixture viscosity against solid volume fraction is compared with the models in Ishii [28]. The three distinct regimes, where mixture viscosity increases in different rates are observed. Furthermore, for large shear-rates, the effective mixture viscosity is very small, and as the shear-rate decreases, the effective mixture viscosity increases rapidly. These results are in line with some observed phenomena [72,73]. So, our results highlight the important features of the new quasi two-phase mass flow model, and hence pave the way for further more complex, and realistic simulations.

Acknowledgments

We thank the reviewers, and the Editor-in-Chief Prof. Spitaleri for their constructive reviews and suggestions that resulted in the substantially improved paper. We gratefully acknowledge the financial support provided by the German Research Foundation (DFG) Germany through the research projects, PU 386/3-1: “Development of a GIS-based Open Source Simulation Tool for Modeling General Avalanche and Debris Flows over Natural Topography” and PU 386/5-1: “A novel and unified solution to multi-phase mass flows”: U_MultiSol.

References

[1] J. Anderson, Governing equations of fluid dynamics, in: J.F. Wendt (Ed.), Computational Fluid Dynamics, Springer, Berlin, 2009.

[2] R.A. Bagnold, Experiments on a gravity-free dispersion of large solid spheres in a Newtonian fluid under shear, Proc. R. Soc. Lond. Ser. A Math. Phys. Eng. Sci. 225 (1954) 49–63.

[3] J. Bathurst, A. Burton, T. Ward, Debris flow run-out and landslide sediment delivery model tests, J. Hydraul. Eng. 123 (5) (1997) 410–419.

[4] F. Battella, T. Bisantino, V. D’Agostino, F. Gentile, Debris-flow runout distance: Laboratory experiments on the role of Bagnold, Savage and friction numbers, WIT Trans. Eng. Sci. 73 (2012) 27–36.

[5] M. Berti, A. Simoni, Prediction of debris flow inundation areas using empirical mobility relationships, Geomorphology 90 (1) (2007) 144–161.

[6] L. Braat, Debris Flows on Mars: An Experimental Analysis, Master Thesis, University of Utrecht, NL, 2014.

[7] P.P. Cageao, B. Turnbull, P. Bartelt, Experiments on the dynamics of subaerial two-phase debris flows, in: Geophysical Research Abstracts, 2013, 2013EGUGA..15.9254P.

[8] M.J. Castro, E.D. Fernández-Nieto, A.M. Ferreiro, C. Parés, Two-dimensional sediment transport models in shallow water equations. A second order finite volume approach on unstructured meshes, Comput. Methods Appl. Mech. Engrg. 198 (33–36) (2009) 2520–2538.

[9] J.E. Costa, G.P. Williams, Debris-Flow Dynamics, U.S. Geol. Surv. Open File Rep., 1984, 84-606.

[10] G.B. Crosta, H. Chen, C.F. Lee, Replay of the 1987 Val Pola landslide, Italian Alps, Geomorphology 60 (1–2) (2004) 127–146.

[11] T. de Haas, L. Braat, J.R.F.W. Leuven, I.R. Lokhorst, M.G. Kleinhans, Effects of debris flow composition on runout, depositional mechanisms, and deposit morphology in laboratory experiments, J Geophys. Res. Earth Surf. 120 (2015) 1949–1972.

[12] R.P. Denlinger, R.M. Iverson, Granular avalanches across irregular three-dimensional terrain: 1. Theory and computation, J Geophys. Res. 109 (2004) F01014, http://dx.doi.org/10.1029/2003JF000085.

[13] B. Domnik, S.P. Pudasaini, Full two-dimensional rapid chute flows of simple viscoplastic granular materials with a pressure-dependent dynamic slip-velocity and their numerical simulations, J. Non-Newton. Fluid Mech. 173-174 (2012) 72–86.

[14] B. Domnik, S.P. Pudasaini, R. Katzenbach, S.A. Miller, Coupling of full two-dimensional and depth-averaged models for granular flows, J. Non-Newton. Fluid Mech. 201 (2013) 56–68.

[15] G. Fairfield, Assessing the Dynamic Influences of Slope Angle and Sediment Composition on Debris Flow Behaviour: An Experimental Approach (Masters thesis), Durham University, 2011.

[16] T. Faug, B. Chanut, M. Naaim, B. Perrin, Avalanches overflowing a dam: Dead zone, granular bore and run-out shortening, Ann. Glaciol. 49 (2008) 77–82.

[17] M. Griebel, T. Dornseiferand, T. Neunhoeffer, Numerical Simulation in Fluid Dynamics: A Practical Introduction, Society for Industrial and Applied Mathematics, Philadelphia, 1997.

[18] K.M. Hákonardóttir, A.J. Hogg, T. Jóhannesson, M. Kren, F. Tiefenbacher, Large-scale avalanche braking mound and catching dam experiments with snow: A study of the airborne jet, Surv. Geophys. 24 (2003) 543–554.

[19] F. Harlow, J. Welch, Numerical calculation of time dependent viscous incompressible flow of fluid with free surface, Phys. Fluids 8 (1965) 2182–2189.

[20] C. Hirt, B. Nichols, N. Romero, SOLA- A Numerical Solution Algorithm for Transient Fluid Flows, Technical Report LA-5852, Los Alamos National Lab, Los Alamos, NM, 1975.

[21] J. Hudson, P.K. Sweby, A high-resolution scheme for the equations governing 2D bed-load sediment transport, Internat. J. Numer. Methods Fluids 47 (2005) 1085–1091.

[22] O. Hungr, A model for the run out analysis of rapid flow slides, debris flows, and avalanches, Can. Geotechn. J. 32 (4) (1995).

[23] O. Hungr, G.C. Morgan, R. Lellerhals, Qualitative analysis of debris torrent hazards for design of remedial measures, Can. Geotechn. J. 21 (4) (1984) 663–677.

[24] K. Hutter, L. Schneider, Important aspects in the formulation of solid-fluid debris-flow models. Part I: Thermodynamic implications, Contin. Mech. Thermodyn. 22 (2010) 363–390.

[25] K. Hutter, L. Schneider, Important aspects in the formulation of solid-fluid debris-flow models. Part II: constitutive modelling, Contin. Mech. Thermodyn. 22 (2010) 391–411.

[26] K. Hutter, B. Svendsen, D. Rickenmann, Debris flow modelling review, Contin. Mech. Thermodyn. 8 (1996) 1–35.

[27] M. Ishii, Thermo-Fluid Dynamic Theory of Two-Phase Flow, Eyrolles, Paris, 1975.

[28] M. Ishii, One-Dimensional Drift-Flux Model and Constitutive Equations for Relative Motion Between Phases in Various Two-Phase Flow Regimes, Argonne National Laboratory, 9700 South Cass Avenue Argonne, Illinois, 1977, 60439, ANL-77-47.

[29] M. Ishii, N. Zuber, Drag coefficient and relative velocity in bubbly, droplet or particulate flows, AIChE J. 25 (1979) 843–855.

[30] R.M. Iverson, The physics of debris flows, Rev. Geophys. 35 (3) (1997) 245–296.

[31] R.M. Iverson, The debris-flow rheology myth, in: D. Rickenmann, C.L. Chen (Eds.), The 3rd International Conference on Debris-Flow Hazards Mitigation: Mechanics, Prediction, and Assessment, Millpress, 2003, pp. 303–314.

[32] R.M. Iverson, R.P. Denlinger, Flow of variably fluidized granular masses across three-dimensional terrain: 1. Coulomb mixture theory, J. Geophys. Res. 106 (B1) (2001) 537–552.

[33] A.M. Johnson, Debris flow, in: Slope Instability, John Wiley, 1984, pp. 257–361.

[34] C.G. Johnson, B.P. Kokelaar, R.M. Iversion, M. Logan, R.G. LaHusen, J.M.N.T. Gray, Grain size segregation and levee formation in geophysical mass flows, J Geophys. Res. 117 (2012) F01032, http://dx.doi.org/10.1029/2011JF002185.

[35] P. Jop, Y. Forterre, O. Pouliquen, A constitutive law for dense granular flows. Coulomb mixture theory, Nature 441 (7094) (2006) 727–730.

[36] J. Kafle, P.R. Pokhrel, K.B. Khattri, P. Kattel, B.M. Tuladhar, S.P. Pudasaini, Landslide-generated tsunami and particle transport in mountain lakes and reservoirs, Ann. Glaciol. 57 (71) (2016) 232–244, http://dx.doi.org/10.3189/2016AoG71A034.

[37] P. Kattel, J. Kafle, J.-T. Fischer, M. Mergili, B.M. Tuladhar, S.P. Pudasaini, Interaction of two-phase debris flow with obstacles, Eng. Geol. 242 (2018) 197–217, http://dx.doi.org/10.1016/j.enggeo.2018.05.023.

[38] P. Kattel, K.B. Khattri, P.R Pokhrel, J. Kafle, B.M. Tuladhar, S.P. Pudasaini, Simulating glacial lake outburst floods with a two-phase mass flow model, Ann. Glaciol. 57 (71) (2016) 349–358, http://dx.doi.org/10.3189/2016AoG71A039.

[39] P. Kattel, B.M. Tuladhar, Interaction of two-phase debris flow with lateral converging shear walls, J. Nepal Math. Soc. 1 (2) (2018) 40–52.

[40] S. Kern, F. Tiefenbacher, J. McElwaine, The rheology of snow in large chute flows, Cold Reg. Sci. & amp; Technol. 39 (2004) 181–192.

[41] K.B. Khattri, S.P. Pudasaini, An extended quasi two-phase mass flow model, Int. J. Non-Linear Mech. 106 (2018) 205–222, http://dx.doi.org/10.1016/j.ijnonlinmec.2018.07.008.

[42] F. Legros, The mobility of long-runout landslides, Eng. Geol. 63 (2002) 301–331.

[43] S. McDougall, O. Hungr, Dynamic modeling of entrainment in rapid landslides, Can. Geotech. J. 42 (2005) 1437–1448.

[44] M. Mergili, A. Emmer, A. Juricova, A. Cochachin, J.-T. Fischer, C. Huggel, S.P. Pudasaini, How well can we simulate complex hydro-geomorphic process chains? The 2012 multi-lake outburst flood in the Santa Cruz Valley (Cordillera Blanca, Peru), Earth Surf. Process. Landf 43 (7) (2018) 1373–1379, http://dx.doi.org/10.1002/esp.4318.

[45] M. Mergili, J.-T. Fischer, J. Krenn, S.P. Pudasaini, r.avaflow v1, an advanced open-source computational framework for the propagation and interaction of two-phase mass flows, Geosci. Model Dev. 10 (2) (2017) 553–569, http://dx.doi.org/10.5194/gmd-10-553-2017.

[46] M. Mergili, B. Frank, J.-T. Fischer, C. Huggel, S.P. Pudasaini, Computational experiments on the 1962 and 1970 landslide events at Huascaran (Peru) with r.avaflow: Lessons learned for predictive mass flow simulations, Geomorphology 322 (2018) 15–28.

[47] D. Naef, D. Rickenmann, P. Rutschmann, B.W. McArdell, Comparison of flow resistance relations for a debris flows using a one-dimensional finite element simulation model, Nat. Hazards Earth Syst. Sci. 6 (2006) 155–165.

[48] M. Pastor, B. Haddard, G. Sorbino, S. Cuomo, V. Drempetic, A depth-integrated coupled SPH model for flow-like landslides and related phenomena, Int. J. Numer. Anal. Methods 33 (2009) 143–172.

[49] A.M. Pellegrino, A. Scotto di Santolo, L. Schippa, Numerical modeling of a debris flow event occurred in Campania region, Southern Italy: Consideration on the rheological model parameters on the run-out, latest trends in engineering mechanics, structures, Eng. Geol. (2014) 62–71.

[50] A.M. Pellegrino, A. Scotto di Santolo, L. Schippa, An integrated procedure to evaluate rheological parameters to model debris flows, Eng. Geol. 196 (2015) 88–98.

[51] C.J. Phillips, T.R.H. Davies, Determining rheological parameters of debris flow material, Geomorphology 4 (1991) 101–110.

[52] T.C. Pierson, Distinguishing Between Debris Flows and Floods from Field Evidence in Small Watersheds, US Dep. of the Int., US Geol. Survey, Reston, Va, 2005.

[53] M. Pirulli, On the use of the calibration-based approach for debris-flow forwards-analyses, Nat. Hazards Earth Syst. Sci. 10 (2010) 1009–1019.

[54] E.B. Pitman, L. Le, A two-fluid model for avalanche and debris flows, Philos. Trans. R. Soc. Lond. Ser. A Math. Phys. Eng. Sci 363 (2005) 1573–1602.

[55] P.R. Pokhrel, K.B. Khattri, B.M. Tuladhar, S.P. Pudasaini, A generalized quasi two-phase bulk mixture model for mass flow, Int. J. Non-Linear Mech. 99 (2018) 229–239.

[56] S.P. Pudasaini, Some exact solutions for debris and avalanche flows, Phys. Fluids 23 (4) (2011) 043301, http://dx.doi.org/10.1063/1.3570532.

[57] S.P. Pudasaini, A general two-phase debris flow model, J. Geophys. Res. 117 (2012) F03010, http://dx.doi.org/10.1029/2011JF002186.

[58] S.P. Pudasaini, K. Hutter, Avalanche Dynamics: Dynamics of Rapid Flows of Dense Granular Avalanches, Springer, Berlin, New York, 2007.

[59] S.P. Pudasaini, K. Hutter, S. Hsiau, S. Tai, Y. Wang, R. Katzenbach, Rapid flow of dry granular materials down inclined chutes impinging on rigid walls, Phys. Fluids 19 (2007) 053302.

[60] S.P. Pudasaini, S.A. Miller, The hypermobility of huge landslides and avalanches, Eng. Geol. 157 (2013) 124–132.

[61] S.P Pudassaini, J.-T. Fischer, A mechanical erosion model for two-phase mass flows, 2016, arXiv:1610.01806.

[62] S.P. Pudassaini, J.-T. Fischer, A mechanical model for phase-separation in debris flow, 2016, arXiv:1610.03649.

[63] D. Rickenmann, Empirical relationships for debris flows, Nat. Hazards 19 (1999) 47–77.

[64] P. Rognon, F. Chevoir, H. Bellot, F. Ousset, F. Naaïm, P. Coussot, Rheology of dense snow flows: Inferences from steady state chute-flow experiments, J. Rheol 52 (729) (2008).

[65] S.B. Savage, K. Hutter, The motion of a finite mass of granular material down a rough incline, J. Fluid Mech. 199 (1989) 177–215.

[66] L. Schippa, S. Pavan, Numerical modelling of catastrophic events, Int. J. Saf. Secur. Eng. 1 (4) (2011) 403–423.

[67] A. Siviglia, G. Stecca, D. Vanzo, G. Zolezzi, E.F. Toro, M. Tubino, Numerical modelling of two-dimensional morphodynamics with applications to river bars and bifurcations, Adv. Water Resour. 52 (2013) 243–260.

[68] Y.C. Tai, J.M.N.T. Gray, K. Hutter, S. Noelle, Flow of dense avalanches past obstructions, Ann. Glaciol. 32 (2001) 281–284.

[69] T. Takahashi, Debris Flow, in: IAHR-AIRH Monograph Series A, Balkema, Rotterdam, Netherlands, 1991.

[70] T. Takahashi, Debris Flow: Mechanics, Prediction and Countermeasures, Taylor and Francis, New York, 2007.

[71] H. Teufelsbaur, Y. Wang, S.P. Pudasaini, R.I. Borja, W. Wu, DEM Simulation of impact force exerted by granular flow on rigid structures, Acta Geotech. (2011) http://dx.doi.org/10.1007/s11440-011-0140-9.

[72] A. von Boetticher, J.M. Turowski, B.W. McArdell, D. Rickenmann, M. Hürlimann, C. Scheidl, J.W. Kirchner, DebrisInterMixing-2.3: A finite volume solver for three-dimensional debris-flow simulations with two calibration parameters - Part 2: Model validation, Geosci. Model Dev. Discuss. 10 (2017) 3963–3978.

[73] A. von Boetticher, J.M. Turowski, B.W. McArdell, D. Rickenmann, J.W. Kirchner, Debrisintermixing-2.3: A finite volume solver for three-dimensional debris-flow simulations with two calibration parameters-part 1: Model description, Geosci. Model Dev. 9 (2016) 2909–2923, http://dx.doi.org/10.5194/gmd-9-2909-2016.

[74] G.B. Wallis, One-Dimensional Two-Phase Flow, McGraw-Hill, New York, 1969, p. 408.

[75] N. Zuber, J. Findlay, Average volumetric concentration in two-phase flow systems, J. Heat Transf. 87 (1965) 453–468.